Magnetic Characterization of Electrodeposited Nanocrystalline Ni and Ni-Fe alloys

By

Sahar Arabi, B.Sc., M.Sc.

A Thesis
Submitted to the School of Graduate Studies
in partial fulfillment of the requirements for the degree of

Master of Applied Science
Department of Materials Science and Engineering
McMaster University

MASTER OF APPLIED SCIENCE (2011)	McMaster University
(Materials Engineering)	Hamilton, Ontario

TITLE	Magnetic Characterization of Electrodeposited Nanocrystalline Ni and Ni-Fe alloys
AUTHOR	Sahar Arabi, B.Sc. (IUST), M.Sc.(International University Bremen (Jacobs University))
SUPERVISOR	Dr. Marek Niewczas

NUMBER OF PAGES: VII, 118

Abstract

This research study has been devoted to the study of magnetic properties and magnetic transport of nanocrystalline Ni and Ni-15% Fe alloys consisting of randomly oriented grains with an average size of 23 and 12 (nm), respectively. The structures of the deposits were confirmed by the XRD analysis using Rietveld refinement technique. The as-deposited Ni and Ni-15%Fe sample was comprised exclusively of the γ phase with lattice parameter of 3.5270 (nm) and 3.5424 (nm), respectively. The small increase in lattice parameter was attributed to the replacement of iron solutes in the Ni sites in lattice. Texture analysis of nanocrystalline Ni and Ni-15%Fe revealed that textures components of both materials is qualitatively the same and vary in terms of volume fraction. Both material showed strong <100> fibre texture with some contribution of the <111> component. The calculated volume fraction of the <100> and <111> components were respectively 17.157% and 3.201% for Ni and, 22.032% and 6.160% for Ni-15%Fe and the rest being confined to the random texture.

Magnetic measurements show that all samples exhibit low loss hysteresis loops with high permeabilities. The presence of 15%Fe in Ni leads to enhancement of the saturation magnetization (M_s) regardless of the direction of the applied field. M_s shows an increase from 60.169 (emu/gr) in nanocrystalline Ni to 93.67 (emu/gr) in Ni-15%Fe sample at T=2K. No strong temperature–dependence of the magnetization was observed for samples, but the magnetization of the Ni-15%Fe samples at T=2K were slightly higher than that of T=298K. The coercivity values of nanocrystalline Ni-15%Fe were in all cases smaller than that of nanocrystalline Ni samples. Good agreement between random anisotropy model (RAM) theory and experiment for nanocrystalline Ni and Ni-15%Fe samples was observed. The ferromagnetic exchange length (L_{ex}) was larger than the average grain size (D) for samples at all times. The effective magnetic anisotropy constants (K_{eff}) of the nanocrystalline Ni and Ni-15%Fe alloys were measured using the law of approach to saturation. At T=2K, the K_{eff} of Ni-15%Fe samples were measured to be 1.7037×10^5 (erg/cm^3) and 2.71996×10^5 (erg/cm^3) at field parallel and perpendicular, respectively. These values were almost half of the values obtained for nanocrystalline Ni samples 4.66091×10^5 (erg/cm^3) and 4.19703×10^5 (erg/cm^3). Temperature dependence measurements showed that K_{eff} constants decrease with increasing temperature. The angular dependence MR studies on nanocrystalline Ni and Ni-15%Fe resulted in a twofold, and a fourfold symmetric behaviour, respectively. The field dependence MR measured at various sample tilt with respect to the applied field, showed various trends from pure positive MR to pure negative MR, which partially could be explained by magnetocrystalline anisotropy of the samples.

Acknowledgements

First and foremost I would like to acknowledge my supervisor professor Marek Niewczas for his advice, guidance, and critical comments during the course of my study at McMaster University.

This research study has been possible because of contributions from many people. I would like to express my deep appreciation to all of them for the encouragement, knowledge and support they provided during my studies. I am particularly grateful to Dr. James Britten for providing me with experience and mentorship, making it possible for me to run X-ray diffraction measurements and analysing the information afterward. I would also like to thank my fellow group member Qiuping Bian who has shared insight and constructive discussions during this project.

Financial support from the Natural Sciences and Engineering Research Council of Canada and Ontario Research Fund are gratefully acknowledged.

My parents deserve special mention for their inseparable support, dedication, love and persistent confidence in me. My mother, Manizhe Mirtorabi, in the first place is my role model for hard working and my first teacher. My father, Abdollah Arabi, showed me the joy of intellectual pursuit ever since I was a child. Thanks to my dearest sister, Sara, for being unconditionally understanding and encouraging. Finally, I would like to thank my dreariest friend, Hadi Meshgi, for being unbelievably helpful and supportive during the course of my studies at McMaster University.

Sahar Arabi

Hamilton

August 201

Table of Contents

Table of Figures

Chapter 1

Introduction

Metallic alloys exhibiting superior magnetic and magnetoresistive properties have been used in industry for over 100 years. The magnetic properties are dependent on intrinsic or extrinsic properties of materials. Saturation magnetization (M_S) is an intrinsic property, independent of grain size and microstructure but it depends on temperature and composition. Permeability (μ) and Coercivity (H_C) are the extrinsic properties, dependant the grain size and microstructure, but also on grain shape, texture and internal stress. Ni and Ni-Fe alloys have been used as materials for read-write heads, magnetic storage, magnetic actuators, magnetic shielding, and high-performance transformer cores [1]. With introduction of nanocrystalline materials, new synthesis processes of Ni, Ni-Fe and a vast variety of materials were designed and examined. These various techniques includes: gas-condensation [2] sputtering [3], sol_ gel technique [4] and electrochemical deposition. These techniques have lead to fabrication of a wide range of bulk Ni- Fe alloys, nanowires, thin-films and multilayers [5]. Each of these techniques may be advantageous over the others and may lead to different physical properties of synthesized materials. Nanocrystalline Ni-Fe alloys used in the industry are fabricated by rapid solidification technique and the microstructure of these alloys is achieved from controlled crystallization of the amorphous precursor such as nanometre-size Fe, Si, P or Br grains embedded in a residual amorphous matrix. These alloys exhibit good Coercivity (H_C) and Permeability (μ); however the saturation magnetization (M_S) of the base material is reduced due to existence of metalloids. Electrodeposition has proven to be a cost-effective technique that results in growth of Ni-Fe films from aqueous solution only by controlling the electrodeposition variables with no need to alloying. With this technique, deposition can be done under normal temperature conditions and alloys with any size and shape can be produced [6]. Several researches have been done on electrodeposition of Ni-Fe alloys [7, 8, 9, 10, 11]. It has been realized that roughness, texture, grain size and alloy composition play key role in magnetic, mechanical, and corrosion properties of Ni-Fe electrodeposits. These parameters can be varied by changing the electrodeposition conditions. In terms of magnetic properties, in electrodeposited nanocrystalline Ni-Fe alloys with ultra-grain sizes, unlike the rapid solidified ones, high saturation magnetization is not sacrificed and overall magnetic properties are more flexible. However one drawback that still restrains these materials from further use in large volume applications in high efficiency power supplies is their high coercivity. A better understanding of the microstructure of the nanocrystalline Ni–Fe alloys is a critical step in developing these new materials.

1.1 Objective and Research Plan

Development of soft magnetic materials took a faster pace in early 1990s when two considerable observations were noticed about coercivity and saturation magnetization of nanocrystalline materials. In the case of Coercivity it was previously believed that the coercivity increases with increasing grain size, D, following a 1/D relationship. Herzer showed that for a range of nanocrystalline materials made by crystallization from amorphous precursors with grain sizes smaller than 50 (nm), the coercivity tend to decrease following a D^6 relationship reaching values as low as 0.01 (A/cm) at grain sizes of 10 (nm). He subsequently proposed random anisotropy model (RAM) where he theoretically predicted a D^6 relationship between coercivity and the grain size. RAM, not only provides the theoretical basis for understanding the soft magnetic properties of amorphous and nanocrystalline ferromagnets but it has been successfully extended to multiphase systems as well. Nanocrystalline electrodeposited Ni and Ni-Fe alloys also follow the Herzer predicted trend, however it has been realized that the initial drop in the coercivity initiates at grain sizes of about 50 (nm) where coercivity is still about 1.0 (A/cm) and still too high for large number of application. Grain size is believed to be one of the many factors that affect the coercivity. Other includes crystallographic texture, grain shape anisotropy, and impurity content. In order to reach small values of coercivity, the contribution of all these parameters has to be assessed.

In the case of saturation magnetization, the early studies on compacted gas-condensed Nickel , cobalt and iron nanoparticles had shown that, saturation magnetization was decreases with decreasing grain size [12,13,14]. This trend is not followed by dense electrodeposited nanocrystalline Ni and that the value of saturation magnetization was found to be dependent on the grain size, decreasing from 10 (μm) to 10 (nm) [15]. The observed degradation of Saturation magnetization with grain size was later found to be due to surface oxidation of the pores existing between particles. The effect of the structural disorder in the grain boundaries was found to be small to induce changes in saturation magnetization [16]. Superior mechanical properties, makes nanocrystalline materials candidates for applications in which a combination of good magnetic properties and excellent mechanical properties are required [17]. The objective of this research study is to evaluate the contribution of various factors such as composition and crystallographic texture on the magnetic properties (including saturation magnetization, coercivity, remnant magnetization and permeability) of nanocrystalline Ni and Ni-15%Fe alloys at two different temperature of 2K and 298K. The correlation between magnetic and magnetotransport properties and the texture, should provide a better understanding of the effect of the microstructure on magnetic properties which could guide the manufacturing process where superior properties and full potential of these bulk nanocrystalline materials can be achieved. Nanocrystalline Ni and Ni-15%Fe alloys used in the present research study are produced in the form of free standing foils as coatings on the polymer substrates using Integran’s nano electrodeposition facilities. The structure and texture of these materials are determined by x-ray diffraction and their magnetic properties are measured using a Quantum Design PPMS-9T system

1.2 Thesis Outline

The thesis is organized as follows:

In Chapter 2 the author presents the background of the in the field of magnetism. Some basic concepts related to the magnetic properties of soft magnetic nanocrystalline materials are also discussed in order to clarify the mechanisms and various energies that play important role in determining the soft magnetic behaviour. At the end a short introduction of the mechanisms that govern the electrodeposition of nanocrystalline Ni and Ni-Fe alloys is given.

In Chapter 3, a brief introduction of the experimental techniques that have been used for the preparation and characterisation of nanocrystalline Ni and Ni-15%Fe alloys is presented. Complementary structural and magnetic investigation techniques that were employed are also discussed. The central interest of this Chapter consists in representing the effect of composition and temperature on the texture and magnetic properties of the prepared samples.

In Chapter 4, texture and magnetic properties of nanocrystalline Ni and Ni-Fe alloys are studied in dependence on temperature, composition and magnetic field. In the next Section, the random anisotropy model (RAM) on the materials studied is presented followed by a discussion on the parameters affecting its validation. The last part of this Chapter, an investigation on the experimental orientation and field-dependance aniostropic magnetoresistance (MR) of nanocrystalline Ni and Ni-15%Fe samples are presented. A discussion on the origin of soft magnetic behaviour of these nanocrystalline alloys in terms of magnetizing process on the basis of MR and RAM are the concluding words of this research study.

In Chapter 5, the author concludes the thesis and gives some suggestions on future research study.

Chapter 2

Background

Introduction

This Chapter presents the background of the research that has been carried out in the field of magnetism. Some basic concepts related to the magnetic properties of soft magnetic nanocrystalline materials are also discussed in order to understand the mechanisms and factors that play important role in determining the soft magnetic behaviour. At the end a short introduction of the mechanisms that govern the electrodeposition of nanocrystalline Ni and Ni-Fe alloys is presented.

2.1 Magnetism

2.1.1 Magnetic Properties and Units

Source of magnetic phenomena in materials are electrons' orbital and the spin motions. Electron spinning around the axis of itself creates a spin moment directed along the orbits around the nucleus of the atom (See Figure 2.1). Sum of the magnetic moments of each of the constituent electrons including the orbital and spin contributions generates the net magnetic moment of the atom. These moments can cancel out if the pair of electron moments is of opposite direction [18]. Materials in which the electron shells are completely filled are incapable of being magnetized.

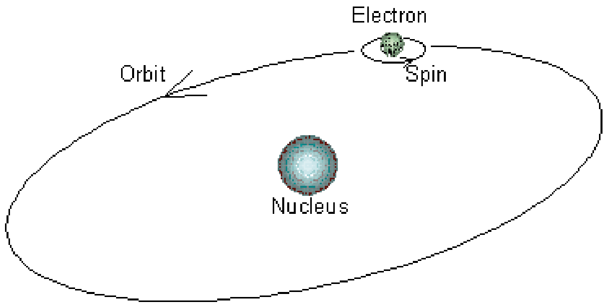

Figure 2.1 Electron moving about the nucleus in an orbit while spinning around its own axis.

All materials depending on the response of their electron and atomic magnetic dipoles to an external field exhibit either of the following magnetism types:

- Diamagnetism,
- Paramagnetism,
- Ferromagnetism
- Antiferromagnetism
- Ferrimagnetism.

The above noted magnetism types are discussed in section 2.2.1

2.1.2 Magnetic Properties

The intensity of the magnetic field is represented by H while the number of dipoles per unit volume of a magnetic material is measured by M or Magnetization. The magnetic flux density of a material is the result of the interaction between the applied field and the field produced by the material itself. I it is defined as B as presented in the equation below (SI system):

$$B = \mu_0(H + M) \tag{2.1}$$

Where μ_0 is the magnetic permeability of a vacuum and is equal to $4\pi \times 10^{-7}$ H/m.

It is worth mentioning that fundamentally H, M and B have the same nature as seen in equation 2.1. However the unit used for the three above mentioned parameters may vary depending on the system of unit being used. Common systems of units include CGS (Gaussian system) and SI system. In CGS system, H and B are expressed in Oersted (Oe) and Gauss (G), respectively. It should be noted that these units are equivalent in CGS system. M is expressed as emu/cm^3 in CGS system. In SI system, H and M are both expressed in A/m while, B is measured in units of (Tesla).

The amount of magnetization produced in a material under influence of an external magnetic field is not only measured by M. There is also another factor which is called susceptibility (χ) and is indicator of variation of M with H:

$$\chi = \frac{M}{H} \tag{2.2}$$

In CGS system, χ is expressed in emu/(cm^3*Oe),while in SI system, χ has the unit of emu/(cm^3•Oe) as M is expressed in the standard CGS units for M and H. However, as M is often expressed as either Oersted or Gauss, χ may also be expressed as a dimensionless parameter.

Magnetic permeability is another parameter which relates the magnetic flux density to the strength of the applied field, and is expressed by:

$$\mu = \frac{B}{H} \tag{2.3}$$

In SI units, permeability is often expressed in relation to the permeability of a vacuum thus, in this case the relative susceptibility (μ_r) is used:

$$\mu = \frac{\mu_0}{\mu_r} \tag{2.4}$$

2.2 Magnetic Materials

Magnetic materials have found to play an undeniable role in history of mankind. The usage of iron and lodestone dates back to 2600 BC while Magnes stones with magnetic behaviour are claimed to be found over 3500 years ago in Asia. With no doubt, inexpensive and abundant iron, made the generation of electricity in large scale possible since 1886. Aside from utility industry, magnetic materials are widely used in computer, communication and in automotive industry. In scientific perspective, it is understood that magnetism is one of the fundamental properties of materials, whether in solid, liquid or gas phase. The term magnetism is described as the behaviour of materials on microscopic level to an applied magnetic field. Although all materials are influenced greater or lesser by the presence of the magnetic field, but the degree of this influence is the key to classify these materials into ferromagnets, paramagnets, diamagnetism and ferromagnets and anti-ferromagnets.

Ferromagnetic materials produce their own magnetic field. Paramagnetism is attracted to the magnetic field while diamagnetism is repelled from it. Materials such as water, aluminum, copper, gases and plastic that are not inherently influenced by a magnetic field are called non-magnetic materials [19,20]. Magnetic state of a material is a function of several parameters such as temperature, pressure, applied magnetic field and its geometry; therefore the material may exhibit more than one form of magnetism by varying any of these parameters [21].

It is now realized that Magnetism appears in different forms, however what interests the modern life of today, are two major groups of ferro- and ferromagnetic materials which are used in almost all major technical fields such as electrical and mechanical motors, high-power electromotors, computer and telecommunication industry, magnetic high-density recording, navigation, aviation and space operations, automation micromechanics, medicine, sensor techniques, magnetocaloric refrigeration, materials testing and household applications.

Each electron possesses a magnetic moment. In atomic perspective, magnetic forces are the resultant of both the orbital motion and spin of the electron at each shell. However, the magnetic moment of the whole atom relies on the electronic configuration of the element and can exhibit either of the below situations:

1. If the magnetic moments of the electrons in the structure cancel each other out, the atom is left with no magnetic moment and therefore a diamagnetic.

2. In case the magnetic moments of the electrons in the structure will not cancel each other out, depending on the nature of the interaction of neighbouring atoms, the atom becomes either paramagnetic, ferromagnetic, ferrimagnetic or antiferromagnetic

Possible magnetism states are presented in Table 2.1 [22].

Table 2.1 Type of magnetism in materials [23].

Type of Magnetism	Susceptibility	Atomic / Magnetic Behaviour		Example / Susceptibility	
Diamagnetism	Small & negative.	Atoms have no magnetic moment	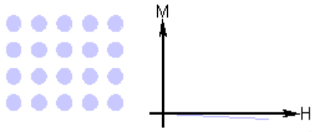	Au Cu	$-2.74\text{x}10^{-6}$ $-0.77\text{x}10^{-6}$
Paramagnetism	Small & positive.	Atoms have randomly oriented magnetic moments	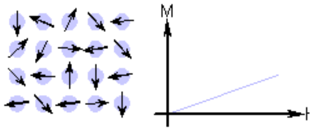	β-Sn Pt Mn	$0.19\text{x}10^{-6}$ $21.04\text{x}10^{-6}$ $66.10\text{x}10^{-6}$
Ferromagnetism	Large & positive, function of applied field, microstructure dependent.	Atoms have parallel aligned magnetic moments	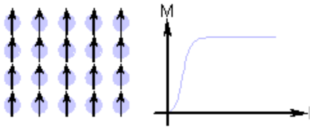	Fe	~100,000
Antiferromagnetism	Small & positive.	Atoms have anti-parallel aligned magnetic moments	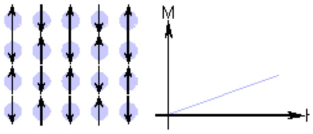	Cr	$3.6\text{x}10^{-6}$
Ferrimagnetism	Large & positive, function of applied field, microstructure dependent	Atoms have mixed parallel and anti-parallel aligned magnetic moments	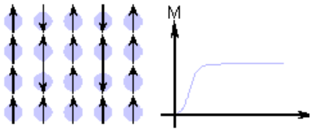	Ba ferrite	~3

2.2.1 Diamagnetic Materials

Almost all materials have the tendency to resist the external field and being repelled by it and therefore exhibiting Diamagnetism behaviour. When exposed to an external field, these materials produce a magnetization in the opposite direction of the applied field according to Lenz’s Law [24]. In diamagnetic materials no unpaired electrons exist, therefore the atoms have no net magnetic moment and the overall magnetization of the material comes from the electrons' orbital motions that can be explained as follows: When a material is exposed to an external magnetic field, its electrons experience two forces: The Coulomb attraction to the nucleus and a Lorentz force from the magnetic field. The latter depends on the orbiting direction of the electron. This Lorenz force may cause the electrons to pull away from the nucleus or get them closer to it. According to Lenz's law, the orbital magnetic moments that were aligned opposite to the field would increase and the ones aligned parallel to the field would decrease. As a result, a small bulk magnetic moment opposite to the direction of the magnetic field is created that leads to the repulsion of that material from the field. However it should be noted that all materials undergo this orbital response, but in paramagnetic and ferromagnetic substances, the diamagnetic effect is partly ignored by the stronger influence of the unpaired electrons [25, 26,27].

2.2.2 Paramagnetic Materials

Paramagnetic materials are composed of atoms, with unpaired electrons that cause net magnetic moments. While in case of paired electrons, the Pauli Exclusion Principle necessitates that the electrons magnetic moments should be in opposite directions and cancels each other out. When relaxed, the magnetic moments in paramagnetic materials tend to randomly orient with respect to each other, resulting in a net zero magnetization. However, when exposed to a magnetic field, these moments align toward the field, causing huge positive susceptibilities in the material. It should be noted that due to thermal vibration of atoms, not all the atomic moments will have the chance to align toward the field. The relationship between susceptibility and temperature was realized by Currie and later by Langevin as presented in Currie-Weiss Law below:

$$\chi = \frac{C}{(T-\theta)} \qquad (2.5)$$

where: C is Curie constant, T is temperature and θ is material constant. θ is zero for a perfectly paramagnetic material [25]. Figure 2.2 shows the temperature dependence of the magnetic susceptibility in para, ferro and antiferromagnets. The theory of Paramagnetism led subsequently to the development of the theory of ferro and ferrimagnetism.

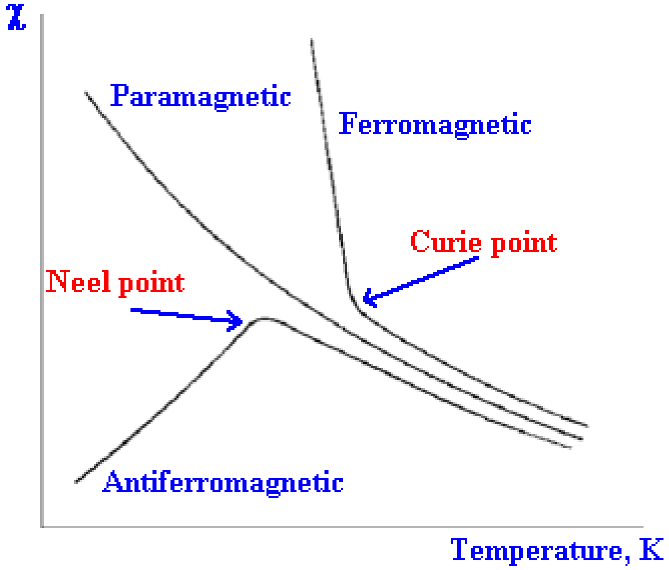

Figure 2.2 Variation of susceptibility with temperature for paramagnetic, ferromagnetic and antiferromagnetic materials [28].

2.2.3 Ferromagnetic Materials

Ferromagnetic materials are analogous to paramagnetic ones in having unpaired electrons that build up a net magnetic moment in their atom. However in ferromagnetic materials the magnetic moments build powerful internal fields that are strong enough to resist the thermal vibration effect in randomizing them and therefore the magnetic movements align parallel to the atoms surrounding them through exchange interactions and create regions called domain [29]. Aside from the tendency of electrons' intrinsic magnetic moments to be parallel to an applied field, one more factor affects this behaviour. To maintain a lowered energy state, the material maintains the parallel orientation of magnetic moments even when the applied field is removed [30,31]. Fe, Co and Ni are the three elements that exhibit ferromagnetic property at room temperature. Six more elements in the lanthanide series including (Gd, Tb, Dy, Ho, Er and Tm) become ferromagnetic at $T = 20^oC$ and subzero temperatures. Several compounds and solid solutions can be processed out of these materials, and therefore the number of magnetic materials can be infinite. The susceptibility of these materials is very large in comparison with paramagnetic ones. As seen in Figure 2.2, the overall trend is that the susceptibility decreases with increasing temperature; however it is apparent that after a certain temperature this trend accelerates sharply. This point is called the Curie temperature at which thermal vibrations of the atoms overcomes the exchange interaction and beyond this point, the ferromagnetic material becomes paramagnetic. Equation 2.5 (Curie-Weiss Law) is true beyond Curie temperature for ferromagnetic materials [24].

2.2.4 Antiferromagnetic Materials

In antiferromagnetic materials, the exchange interactions present among atoms result in anti parallel magnetic moments in neighbouring atoms [24]. These materials act almost the same as paramagnetic materials in having no net magnetization. This effect is due to the structure of antiferromagnets, which is composed of two associated sublattices of atoms in which the magnetic alignments are opposite to each other. The characteristic temperature of the antiferromagnetic materials is called “Neel temperature” (See Figure 2.2) beyond which the magnetic moments of atoms will orient randomly and in fact the material becomes paramagnetic.

2.2.5 Ferrimagnetic Materials

Ferrimagnetic materials similar to antiferromagnetic ones, exhibit magnetization at room temperature and saturated domains; however with an unzero net magnetic moments that leads to an overall magnetization which is of course less than it would be for ferromagnetic materials as not all the atoms counteract the dominant direction of magnetization. These types of magnetic materials contain ionic compounds, such as oxides, i.e. lodestone or magnetite (Fe_3O_4) that belongs to the class of ferrites [32].

2.3 Ferromagnetism

2.3.1 Magnetization

As mentioned in Section 2.2.3, ferromagnetic materials in their demagnetized states are composed of domains that are oriented the way that the final net zero magnetization is not equal to zero. In process of magnetization, domains that are closely oriented in the direction of the magnetic field turn and join those that are placed parallel to the applied magnetic field at the expense of other domains. This process continues till the domains are mostly oriented closest to the direction of the applied field. At this stage, the domains are still oriented along their easy axis and in order to reach saturation, the applied field should shift the direction of magnetization to a non-easy direction.

2.3.2 Magnetic Hysteresis

When a ferromagnetic material is magnetized in one direction, it will not become demagnetized by removing the applied magnetic field, unless it is exposed to a field in the opposite direction. A hysteresis loop is produced when an alternating magnetic field is applied to the material. This curve depicts the magnetization behaviour of the material which is magnetized to saturation under applied field H, first in one direction and then in the opposite direction. Hysteresis loop of a typical ferromagnetic material is shown in Figure 2.3.

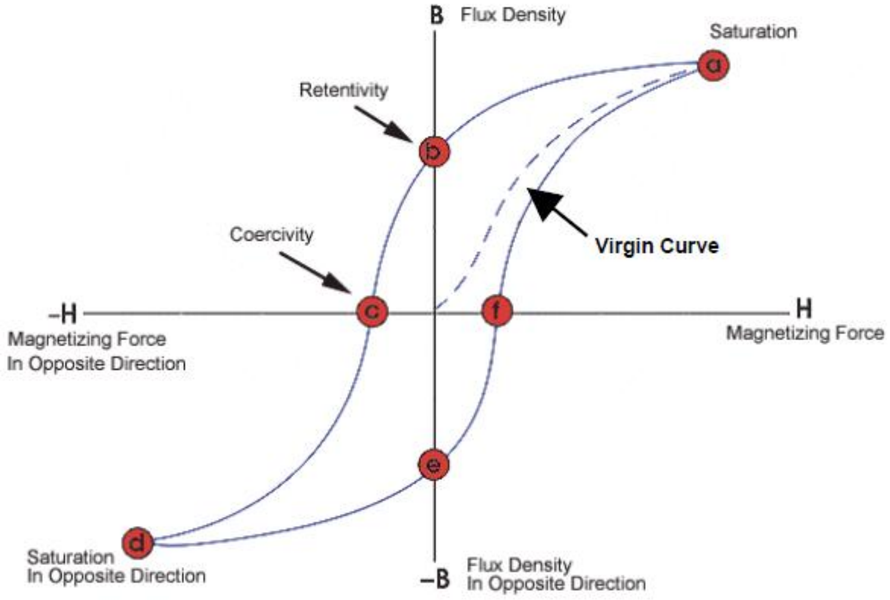

Figure 2.3 A magnetic hysteresis loop. Points (a) and (d) show the saturation magnetization of the material, (b) and (e) show the remnant magnetization, and (c) and (f) show the coercivity [33].

Several important properties can be derived from the hysteresis loop such as saturation magnetization (M_S), the remnant magnetization (M_R) and the coercivity (H_C).

The saturation magnetization (M_S) of a material is a function of the strength of dipoles or the composition, the density of the atomic packing and the degree of alignment of the magnetic domains that are built in the material. In presence of the thermal vibration of atoms the complete alignment of the dipoles is impossible. Thus, the saturation magnetization reaches its highest value when these vibrations are least at T=0K and tend to decrease as temperature increases.

Remnant magnetization (M_R) is the remaining magnetization in the material when the applied magnetic field is removed.

Coercivity (H_C) of the material is the measure of the reverse magnetic field required to vanish the magnetization from the material. Large coercivity values means the material is a "harder" magnet. The softer the ferromagnet, the lower the value of the coercivity. "Virgin curve", shows the magnetization behaviour of a material from its demagnetized state (zero magnetization at zero fields). To demagnetize a material after magnetization, it should be annealed above its Curie temperature and then quenched in absence of a magnetic field.

The hysteresis loop may have different shapes: round, flat and rectangular, which are described by the ratio of M_R/M_S. If this ratio is <0.5 then the hysteresis loop is flat; when $0.6 < M_R/M_S < 0.7$ the loops is round and when this ratio is approximately 0.9 the hysteresis loop is rectangular.

A flat hysteresis is resultant of the early rotation of the spins with a preferred direction perpendicular to the later magnetic flux direction in remagnetization cycle process. A rectangular hysteresis loop is attained in the case where a preferred direction parallel to the later magnetic flux direction is available and the magnetization is more or less ruled by Bloch wall movement (which will be discussed in detail in next Section) and therefore no spin rotation processes is needed.

2.3.3 Domain Theory

Pierre Weiss justified the high susceptibility and magnetic hysteresis curves of ferromagnetic materials below their Curie temperature by formation of regions where atomic dipoles self align with their neighbouring atoms and behave similar to little permanent magnets. These regions bond together and create regions of uniform magnetic alignment which are called magnetic domains or Weiss domains [24]. These domains are known to be magnetically saturated as in these regions all atoms are perfectly aligned, and therefore has the highest possible magnetization. Such domains and their boundaries can be identified by means of various scientific experiments one of which is magnetic force microscopy [34,35,36,37]. In ferromagnetic materials, there is a misalignment between these domains which results in lower magnetization for the overall material thus, reaching a Maximum saturation magnetization and external magnetic field is necessary for alignment of moments. In absence of an applied magnetic field, in a ferromagnetic material, the moments are magnetized along their easy axes of magnetization. In case of too many molecules, the domain becomes unstable and to reach a stable condition with lower energy, it splits into domains with opposite directions. The demagnetizing fields around the uniformly magnetized regions are responsible for magnetostatic energies [24].

In case of having a single rectangular domain with uniaxial anisotropy, the free poles at both ends of the domain, create a magnetic field from North to the South Pole. By applying an external magnetic field, an induced magnetic field in opposite direction of the interior magnetic field is produced which is responsible for the unfavourable magnetostatic energies in the sample [38]. The trend to minimize such energies is to decrease the area of the free poles and construct a second domain with anti-parallel magnetic moment to form a dipole that consequently decrease the strength of the external field (see Figure 2.4 (b)) [24].

However as making new domain walls itself requires energy, after a certain point, creating new domains with opposite dipole directions is no longer energy-favourable, and from this point magnetostatic energies can be lowered via formation of “closure” domains at free surfaces in crystal systems that contain perpendicular easy axes of magnetization (see Figure 2.4 (d))

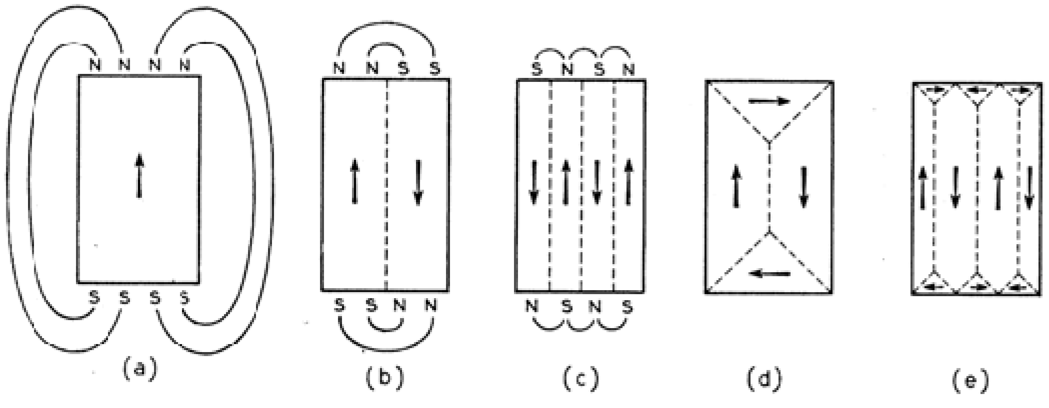

Figure 2.4 The origin of domains [39].

When exposed to an external field as depicted in Figure 2.5, domain boundaries shift leading to a growth and dominancy of domains with alignment toward the magnetic field.. The term super saturation is referred to the situation when under strong magnetization, the predominant domain, suffuses all available domains and makes one dominant domain. When heated above the Curie temperature, the thermal vibration of the atoms results in disorganization of the magnetic domains and vanishing of the magnetic properties [40].

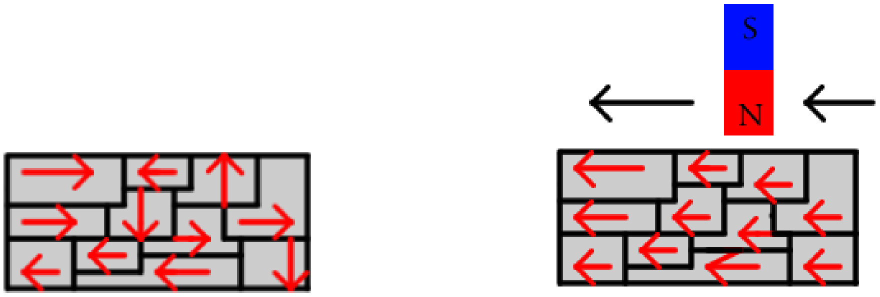

(Unmagnetized) (Magnetized)

Figure 2.5 Domain structure in the a) unmagnetized and b) magnetized state

2.3.4 Energy Consideration for the Magnetic Domain

It was earlier mentioned that the magnetic domains are shaped to lower the energy state of the material. Basis for modern domain theory was first presented by Landau and Lifshitz. They estimated the theoretical domain structure based on a minimum energy concept. The energy of a crystal is sum of several free energy terms [41,42, 43].

$$E = E_{EX} + E_K + E_\lambda + E_D + E_H \qquad (2.6)$$

Where, E_{ex} is the Exchange energy, E_k is the Magnetocrystalline anisotropy energy, E_λ is the Magnetoelastic energy, E_D is the Magnetostatic energy and E_H is the Zeeman energy. These energies are described below in brief.

Magnetocrystalline anisotropy energy: The most common type of anisotropy in magnetic materials that comes from the spin electron movement is magnetocrystalline anisotropy. The magnetic materials are not isotropic and there are some directions in their crystal lattice that are magnetized easier than some other directions. Being magnetized in the direction of "easy" axis decreases the magnetocrystalline anisotropy energy. This energy will be discussed in detail later in this Section 2.3.5.1.

Magnetoelastic energy: The change in the crystals dimensions as a result of magnetization is called magnetostriction, which is responsible for Magnetoelastic energy. This phenomenon creates elastic strains in the crystal lattice. The direction of magnetization which keeps these strains energies as low as possible is favoured.

Magnetostatic energy: This energy is resultant of the interaction between the magnetic field produced by the magnetization in one part of the material and the other part of the material. Creation of magnetic domains in magnetic materials is resultant of presence of such energy. To minimize this energy, closed magnetization loops are to be made while the magnetization on the material edge is parallel to the surface.

Zeeman Energy: This energy is resultant of the interaction between the material and the external applied field [24].

2.3.5 Anisotropy

The hysteresis loop of a magnetic material provides information on the magnetization process in that material. With changing the orientation of the object with respect to the magnetic field, its hysteresis loop may change. This effect is due to magnetic anisotropy that results from the fact that materials tend to be magnetized in some directions easier than other directions. This direction is so called the” easy” direction. Opposed to this direction exist a “hard” axis which is the direction along which a magnetization of a material is most difficult. The term magnetic anisotropy energy shows the dependence of the internal energy on the direction of the inner magnetization in the material. Two mechanisms of magnetic dipolar interaction and spin-orbit interactions are responsible for this energy [44]. Figure 2.6 shows the magnetization behaviour for Nickel when magnetized along its easy and hard axes.

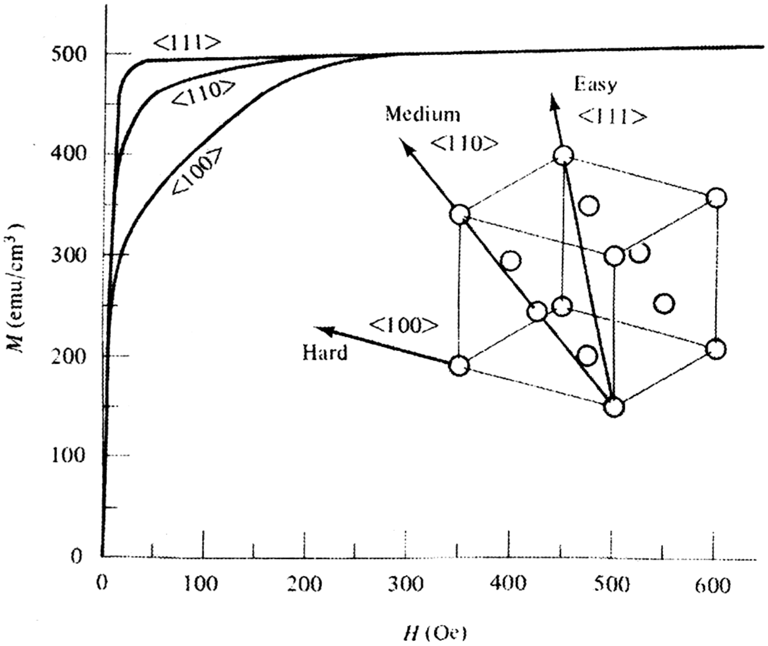

Figure 2.6 Magnetization curve for a single crystal of Ni along its hard and easy axis [24].

The amount of energy required to shift the magnetization of a material from its easy direction to its hard direction is known as anisotropy energy. In general, the crystallographic, shape and stress anisotropy are three main sources of anisotropic energy that are induced in the sample through material preparation. These terms are fully described next.

2.3.5.1 Crystallographic Anisotropy

Crystallographic anisotropy is the only intrinsic source of the anisotropy in a material that arises from the preference of the atoms to align their dipoles in a certain direction with respect to their crystallographic configuration. As mentioned before, the spins are coupled to orbital via the spin-orbital interaction, under crystal lattice influence. This interaction generates a small orbital momentum in the material that couples the magnetic moment of both the spin and the orbital to the crystal axes. The resultant is an energy that depends on the orientation of the magnetization relative to the crystalline axes and in fact reflects the symmetry of the crystal. The crystallographic anisotropy in cubic crystals is described as below:

$$E_c = K_0 + K_1(\alpha_1^2\alpha_2^2 + \alpha_2^2\alpha_3^2 + \alpha_3^2\alpha_1^2) + K_2(\alpha_1^2\alpha_2^2\alpha_3^2) + \ldots \qquad (2.7)$$

Where α_i constants are the cosines between the direction of magnetization and the crystal axes. K_0, K_1 and K_2 are the cubic anisotropy constants, in ergs/cm^3 [24].

K_0 is the angle-independent constant and is usually ignored because the change in the energy E when the M_S vector rotates from one direction to another is important here. K_2 is often much smaller than K_1 and K_N values greater than K_2 are considered negligible. The direction of magnetization which leads to minimization of the value of E_C is considered as the easy axis.

It is worth mentioning here that, although the fundamental of crystallographic anisotropy is understood, limitations in knowing the specifics of this relations has made the theoretical prediction of the anisotropy energy impossible, thus no precise rules exist for determining these constants and these values are generally obtained only by experiment.

2.3.5.2 Magnetic Dipolar Anisotropy (Shape Anisotropy)

One of the most important sources of magnetic anisotropy in thin films is the shape anisotropy. The source of this anisotropy is when a material is magnetized; free poles are formed at the surface of it, which result in formation of magnetostatic energies caused by demagnetizing field inside the material. This anisotropic demagnetizing field in ellipsoidal ferromagnetic samples is described as: $\mathbf{H}_d$ = -N.$\mathbf{M}$. Where M is the magnetization vector and N is the shape-dependent demagnetizing tensor. All tensor elements are considered as zero in thin films except for the direction perpendicular to the layer: $N^{\perp}=1$

It is known that magnetostatic energy equation can be described by Equation 2.8 below:

$$E = \frac{\mu_0}{2V}\int \vec{M}.\vec{H}_d.\,dv \qquad (2.8)$$

Where μ_0 is the permeability of the vacuum. Thus the anisotropy energy per unit volume V of a film can be obtained as:

$$E = \frac{1}{2}\mu_0 M_S^2 \cos^2\theta \tag{2.9}$$

Where M_S is the saturation magnetization and θ is the angle between magnetization and the film normal. As the free poles are commonly formed over a long distance on the surface, the demagnetizing energies to magnetize the material along the short axis are higher than the long axes. So being magnetized over the long axis is favoured in bulk materials. Only in spherical particles, the shape anisotropy effects are unobtainable. It is also apparent from equation 2.9 that the energy contribution favours an in-plane preferential orientation for the magnetization.

2.3.5.3 Stress Anisotropy

Reaching Saturation Magnetization in a material often results in changes in the material's dimensions, this effect is known as magnetostriction (λ).

$$\lambda_S = \frac{\Delta l}{l} \tag{2.10}$$

Where λ_s is the magnetostriction constant, which is usually a small value ($<10^{-4}$). As mentioned earlier, Magnetostriction is resultant of the interaction between the magnetic moment of atom and the shape of its electron cloud.

Magnetostriction in a material causes the electron cloud of the material to become elliptical. The long direction of the ellipse is along the magnetization direction. As a result, the neighbouring atoms are repelled in one direction while others are relatively unmoved; thus changing the direction of the magnetization causes the dimensions of the material to change. Therefore the stresses that acts opposite to magnetostrictive tendency of the material makes the magnetization in that direction harder which results in formation of hard axis. On the other hand, stresses that agree with the magnetostrictive effect in material ease the magnetization in that direction. Stress anisotropy energy per unit volume for a material under uniaxial stress σ is expressed as below [24]:

$$E = \frac{3}{2}\lambda_s \sigma \sin^2 \theta \qquad (2.11)$$

2.4 Soft Magnetic Materials

Now knowing the domain wall motion and the domain magnetization terms, soft magnetic materials can be easily described. Those ferromagnetic materials where the occurrence of rotation of domain wall happens in fields as small as $<10^3$ A/m are called soft [45]. The flux density in soft magnetic materials is dominated by the contribution of magnetization. These materials are classified in the following categories

(a) Fe-Si steels: Iron is known as soft magnetic metal with relatively high saturation magnetization and low magnetocrystalline anisotropy of 2.2 (Tesla) and 48 (kJ/m^3), respectively. Introduction of silicon to iron, despite of decreasing the saturation

magnetization value leads to successfully increasing of the electrical resistivity and mechanical strength of alloy as well as cutting down the core losses.

(b) Fe-Ni alloys: These alloys commonly called as permalloys are widely known as a family of Fe-Ni_3 FCC compound containing Nickel percentage of about 35 to 100. Four major categories within this family are Supermalloys, 65%, 50% and 36% Nickel, each with rather different magnetorestriction, anisotropy and hysteresis characteristics, which make them good candidates in different applications.

(c) Fe-Co alloys: These so-called Permendur alloys, exhibit saturation magnetization values as high as 2.4 (Tesla) and a low magnetic anisotropy value of about -10kJ/m3. These alloys are considered expensive due to cobalt content, and are used in applications where a high flux versus low weight is demanded over the AC loss and cost. One application of these materials is in generators of aircraft power systems.

(d) Soft Spinel ferrites: These soft ferrites with Fe_3O_4 spinel structure exhibit very high resistivity and corrosion resistance, low saturation magnetization and Curie temperature. These materials are mostly used for high frequency applications. The two common categories of ferrites are Mn-Zn and Ni-Zn ferrites.

(e) Amorphous alloys: The evolution of these families of alloys dates back to 1934 when the first metallic glass was made by Kramer by chemical vapour deposition. Unlike what was believed before that amorphous state could not exhibit ferromagnetic properties due

to lacking long range ordering, it was shown by Gubanov [46] that glassy materials can be ferromagnetic and can be thought as an extended liquid state with some aspects of solid state. These alloys are divided into families of bulk amorphous alloys, glass covered amorphous micro wires and thin films depending on their shape and method of production.

(f) Nanocrystalline magnetic alloys: Fast casting process the amorphous structure leads to an unstable structure where the amorphous state always tends to reach a more stable state by different trends that would eventually change the structure and the properties of the material. In addition to this, minimizing the magnetostriction by creating a two phase system, raised up the idea of partially crystallized structures. This idea did not come true until 1988 where Yoshizawa et al. reported a new family of Fe-Si-B soft magnetic materials called FINEMET [47] with high saturation magnetization (1.24 (Tesla)), low coercivity (0.5 (A/m)) and high permeability (105 at 1kHz). Later on ,a Fe-Zr-B based nanocrystalline alloy called NANOPERM was introduced by Suzuki et al. that exhibited saturation magnetization of as high as 1.6 (Tesla) [48]. Both grain sizes of the aforementioned alloys were around 10 (nm). HITPERM is a high temperature version of NANOPERM that contains high cobalt content [49].

2.4.1 Origin of Soft Magnetism in Nanocrystalline Materials

The essence of soft magnetic behaviour in nanocrystalline materials as well as amorphous alloys is in the effective magnetic interactions between various magnetic dipoles inside the matter in length scales determined by the structural properties. The structure of these materials is assumed to be disordered in comparison with arranged polycrystalline or single crystalline materials which lead to a randomness in the interaction of their magnetic dipoles. This randomness can be either the random isotropic exchange or the random anisotropy, where the former is ineffective on the magnetic properties while the latter strongly affects the magnetic properties through breaking the rotational symmetry of the associated interaction energy. The asymmetry of the structure produces local fields which influences primarily the magnetic moments inside the matter and create local random magnetocrystalline anisotropies. The strength of these local anisotropies is orientation-dependant and as they do not cancel each other out, they result in a balance between anisotropic and exchange forces in the matter. This give rise to a certain magnetic behaviour over various length scales. However there is a specific length scale, almost in the order of domain wall, in which anisotropy and exchange interaction come to a balance. This length is called ferromagnetic exchange length and is described by equation 2.12 below:

$$\mathrm{L_{ex}} = \varphi \sqrt{\frac{\mathrm{A}}{\mathrm{K_1}}} \qquad (2.12)$$

Where K_1 is the anisotropy constant, and φ is a parameter which arises from the rotation of spins over the exchange length in the order of one and A is the exchange constant that is described as below:

$$A = \frac{M_s\, D_{sp}}{2g\, \mu_B} \tag{2.13}$$

Where D_{sp}, g, and μ_B are the spin wave stiffness constant, gyro-magnetic ratio and the Bohr magnetron, respectively.

According to Hezer, below the L_{ex} scale, direction of the magnetization cannot vary significantly. The order of the domain wall width can be determined when $D>L_{ex}$. This value has been determined around $L_{ex} \simeq$ 20-30 (nm) for Fe-based alloys previously. Both amorphous alloys ($D \simeq$ atomic scale) as well as nanocrystalline alloys ($D \simeq$ 5-25 (nm)) follow this behaviour. The exchange length consequently defines an exchange volume with an "easy" direction of magnetization that results in accumulating the random anisotropies.

The number of nanograins existing in the exchange volume of nanocrystalline magnetic material (N) can be obtained via Equation 2.14:

$$N = \left(\frac{L_{ex}}{D}\right)^3 \tag{2.14}$$

This mechanism is understood by the frame research study of Herzer theory [50,51,52,53], which was initially introduced for amorphous alloys and later on expanded to the two-phase nanocrystalline alloys. According to Herzer theory, polycrystalline materials composed of large grains where the magnetization is dominated by the magnetocrystalline anisotropy K_1, and reasonably the magnetization vector in each grain is in the direction of the easy magnetization. However in the case of randomly orientated ultrafine grains where the exchange length is larger than the nanograin diameter (D), the magnetization vector is prohibited from orienting along the easy magnetization direction of the grain by exchange interactions. This causes the anisotropy constant to get reduced to an effective anisotropy K_{eff} described as mean fluctuation amplitude of the magnetocrystalline anisotropy K_1 of each individual grain:

$$K_{eff} = \frac{K_1}{(N)^{1/2}} \tag{2.15}$$

In nanocrystalline materials where N is large, K_{eff} becomes much smaller than K_1, resulting in averaging out of the magnetic anisotropy of each grain. This leads to excellent soft magnetic properties. Figure 2.7 illustrates a schematic of the Herzer random anisotropy mechanism for nanocrystalline magnetic alloys. It is apparent that the effective magnetocrystalline anisotropy of exchange coupled nanograins with average size D and crystalline phase of volume V_x is resulting from averaging the anisotropy constant over all nanograins available in the exchange volume (the shaded area).

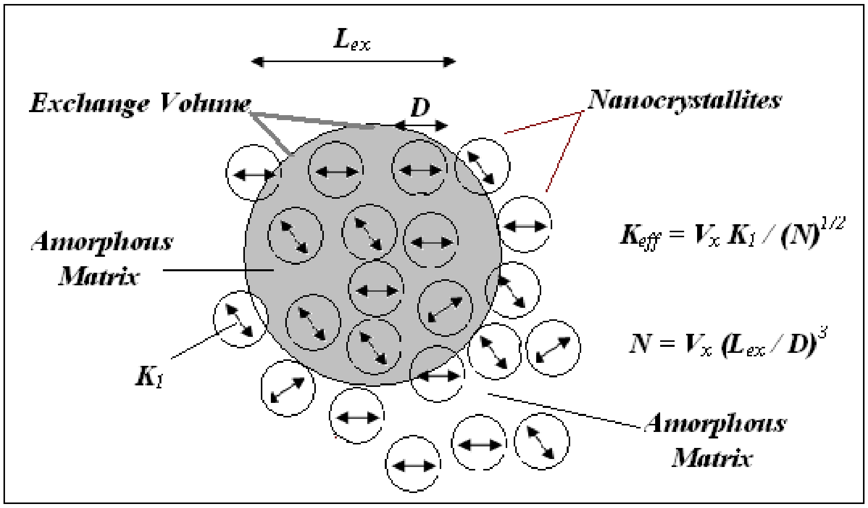

Figure 2.7 Schematic representation of random anisotropy model for nanocrystalline magnetic materials in [52].

By taking into account the statistical fluctuations, the effective anisotropy constant is calculated as below:

$$K_{eff} = \frac{V_x K_1}{(N)^{1/2}} \tag{2.16}$$

In above equation, N is the number of exchange coupled nanograins achieved as following:

$$N = V_x \left(\frac{L_{ex}}{D}\right)^3 \tag{2.17}$$

In the case of binary nanocrystalline alloys the same as the systems composed of two phases where nanograins are surrounded in a soft magnetic amorphous matrix, the effective anisotropy density can be derived by:

$$K_{eff} = \frac{V_x^2 \, K_1^4 \, D^6}{(A)^3} \qquad (2.18)$$

Similarly, in the systems where magnetocrystalline anisotropy dominates the magnetization behaviour, the Coercivity can be achieved by equation 2.19 below:

$$H_c = P_c \frac{K_{eff}}{M_s} = P_c \frac{V_x^2 \; K_1^4 \; D^6}{(A)^3 . \; M_s} \qquad (2.19)$$

The above expressions are the most important predictions of the Herzer random anisotropy model (RAM), in which the effective anisotropy and coercivity are related to the grain size to the power of six. In Figure 2.8, coercivity and permeability are plotted as function of average grain size for Fe-based nanocrystalline alloys in addition to amorphous and conventional polycrystalline soft magnetic materials. Nanocrystalline materials reside in the gap between amorphous and conventional polycrystalline alloys. The trend can also be observed in the grain size dependence of coercivity H_C (K_{eff}) and permeability μ ($1/ K_{eff}$). The deviation from the grain size dependence in equation 2.19 has been attributed to existence of the additional crystalline phases and/or the magneto-elastic and induced anisotropies.

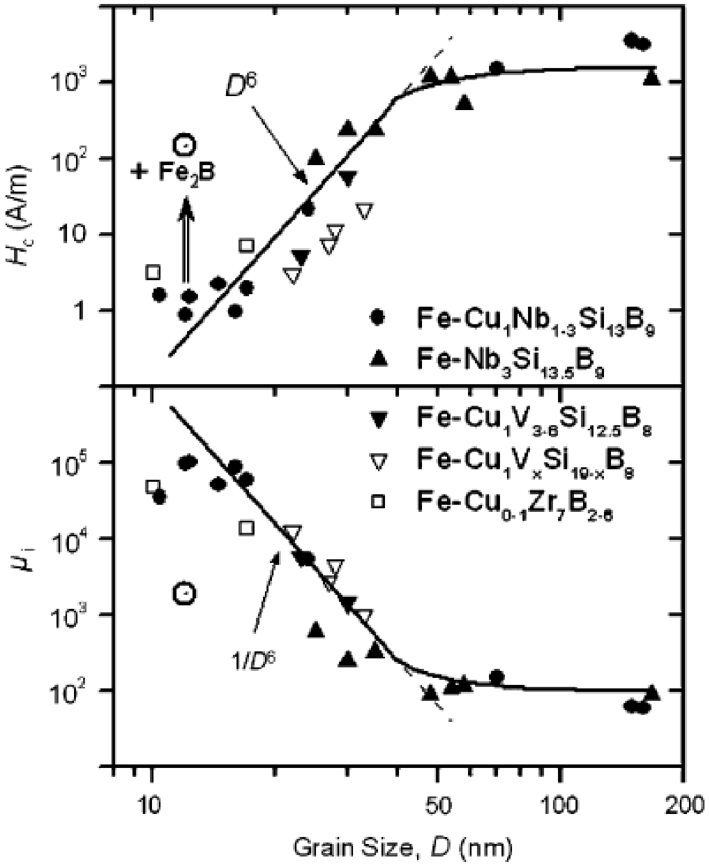

Figure 2.8 Coercivity (H_C) and initial permeability (μ_i) variation with average grain size for various Fe-based nanocrystalline alloys[53].

2.4.2. Law of Approach to Saturation

Magnetic behaviour of nanocrystalline alloys is directly related to their magnetocrystalline anisotropy which favours or disfavour the random anisotropy model system. To better investigate these properties, it is essential to directly measure the effective magnetocrystalline anisotropy constant K_{eff}. This value can provide information on the existence of magnetocrystalline anisotropy in the sample. The principle of obtaining the effective magnetocrystalline anisotropy constant value (K_{eff}) is through the law of approach to saturation which is explained below.

As described earlier, due to ferromagnetic exchange interactions, the effective magnetic anisotropy (K_{eff}) being the mean fluctuation amplitude of K_1 cannot possess a cubic symmetry, and may show a preferred axis of magnetization. Therefore, the specimen under investigation may be assumed as a system with many randomly oriented magnetic domains with uniaxial anisotropy, for each domain of volume (V) and anisotropy of (K_{eff}). Benefiting from this approach through resembling the magnetization of our specimen with magnetization of a uniaxial polycrystalline material and by using the law of approach to saturation, the value of (K_{eff}) can be measured.

In 1940-1941 Brown [54,55] published his revolutionary papers on the theory of micromagnetism of ferromagnetic materials where the spin states in domain walls, at nucleation processes and in the neighbourhood of lattice imperfections in ferromagnetic crystals are described. For the field dependence of the deviation ΔM from saturation magnetization, (M_S), the following power series were proposed:

$$\Delta \boldsymbol{M} = \frac{\boldsymbol{a_1}}{\boldsymbol{H}} + \frac{a_2}{H^2} + \qquad (2.20)$$

The coefficient $\frac{a_1}{H}$ was shown to be caused by the dislocation dipoles if the distance between the two dipole dislocations is smaller than the exchange length.

Neel showed that $\frac{a_1}{H}$ term may arise from nonmagnetic inclusions as well. Later on measurements of the high-field magnetization curves of rapid solidified amorphous alloys showed that the law of approach to saturation of these materials is also described by the power series (2.20). This treatment were further expanded to different nanocrystalline alloys, such as various Fe–Cu–Nb–Si–B, Fe-Zr-B, FeNdB, and $Fe_{100\sim x}$ Si_x alloys [56, 57,58].

Appearance of the law of approach to saturation magnetization used in different research is different since it is an experimental achieved expression. However, the most common form is expressed as:

$$M = M_s \left(1 - \frac{a_1}{H} - \frac{a_2}{H^2} - \frac{a_3}{H^3} \ldots\right) + \chi H \qquad (2.21)$$

Where M is the spontaneous magnetization in an applied magnetic field H, M_s is the saturation magnetization, a_1 and a_2 are constant coefficients and χ is the high field susceptibility resulting from the increase in the spontaneous magnetization by the application of the field. It is observed that the main contributions in equation 2.21 are $\frac{a_1}{H}$ and $\frac{a_2}{H^2}$ terms. In fact the $\frac{a_1}{H}$ is due to point-like defects and intrinsic Magnetoelastic fluctuations where the term, $\frac{a_2}{H^2}$ is to some extent due to Magnetoelastic interaction of quasi dislocation dipoles, but mostly due to non-compensated anisotropy energy

In nanocrystalline structures, large amount of extended imperfections such as triple junctions, dislocations and stacking faults are present. The internal stresses of dislocations cause inhomogeneous spin states that lead to significant deviations from saturation in the crystals containing these defects.

The method for obtaining the coefficients $a_1$and a_2 is through fitting experimental curves with this full expression. However, the fitting procedures have resulted in vague coefficients since curve can be fitted with more than one combination of coefficients. To overcome this issue, equation 2.21 was improved to equation 2.22 below to reach more reasonable results with reference to the research study done by Kronmüller [59]::

$$M = M_s \left(1 - \frac{a_1}{\sqrt{H}} - \frac{a_2}{H^2} - \frac{a_3}{H^3} \ldots\right) + \chi H \qquad (2.22)$$

For cubic crystal materials, the coefficient a_2 which is related to magnetocrystalline anisotropy is determined as: [60].

$$a_2 = \left(\frac{8}{105}\right) * (K_{eff}^2/(\mu_0^2 M_S^2) \qquad (2.23)$$

By knowing the values of a_2, K_{eff} values can be calculated from the equation below:

$$K_{eff} = \mu_0 M_S * (105\, a_2/8)^{1/2} \qquad (2.24)$$

Initially, in order to figure out whether equation 2.22 can be applied to analyze the experimental data the experimental Magnetization data are to plotted as a functions of $\frac{1}{\sqrt{H}}$

and $\frac{1}{\mathrm{H}^2}$ for the nanocrystalline Ni-Fe alloys as well as the pure Ni bulk. If the corresponding magnetization plots showed the dependence according to a $\frac{1}{\sqrt{H}}$ -law as well as $\frac{1}{H^2}$-law for certain field ranges then equation 2.22 can be used to fit the experimental data. By deriving the values of a_2 and M_S from fitting, the K_{eff} can be calculated from equation 2.24.

2.5 Anisotropic Magnetoresistance

Magnetoresistivity (MR) is a property of materials to change their electrical resistivity when an external applied field is applied to them. In 1857, William Thomson discovered the anisotropic magnetoresistance in ferromagnetic metals [61]. However, the successful implementation of it as a detection element in magnetic recordings did not occur till the next century. MR is a phenomenon in which the electrical resistance depends on the relative orientation of magnetization and current. MR is mainly due to anisotropic scattering of conduction electrons due to the spin-orbit interaction and the anisotropic scattering probability of carriers [62]. Magnetic tape recording systems have utilized this effect in great deals in position sensing and dead reckoning for huge capacity data storage. The MR effect is a part of the resistivity tensor and can be phenomenologically expressed as [63]:

$$\rho_{\mathrm{long}} = \rho_{\perp} + (\rho_{\mathrm{II}} - \rho_{\perp})\cos^2\varphi \qquad (2.25)\ \mathrm{a}$$

$$\rho_{\mathrm{trans}} = (\rho_{\mathrm{II}} - \rho_{\perp})\sin\varphi\cos\varphi \qquad (2.25)\ \mathrm{b}$$

Equations 2.25 a and b contain traditional MR and planar Hall Effect, respectively. $\rho_{\perp}$ and $\rho_{\boldsymbol{II}}$ are the resistivity for the magnetization perpendicular and parallel to the current independent of crystal axes, respectively and φ is the angle between current and magnetization. It is important to note that both above equations have a twofold symmetry about the current direction with the rotation of magnetization and are related to each other. Recent studies have shown deviation of MR from twofold symmetry. Systems such as manganite [64, 65], (Ga,Mn)As [66,67], as well as in Fe_3O4 films actually have exhibited a fourfold symmetry MR[68].

The origin of this fourfold symmetry is the subject of intensive scientific dispute. The fourfold symmetry in single crystal (GaMn)As films has been attributed to the long-range ferromagnetic phase at $T<T_C$. In high magnetic fields, the phase of antiferromagnetic ordering near the anitiphase boundaries in CuO_2 plane gets coupled and creates fourfold symmetry through help of orthogonal twins and anitiphase boundaries. On the contrary, in magnetite, the fourfold symmetry was observed in fields smaller than the anisotropy field, where as in larger field the twofold symmetry was observed [69, 70].

The fourfold symmetry in half-metallic Fe_3O_4 was found to be due to magnetocrystalline anisotropy [64, 65].

The microscopic physical origin of the high order MR and the evolution from twofold symmetry to fourfold symmetry are not yet well understood and are still under investigation. Several factors, including strain, magnetic field, temperature, annealing and doping may be responsible for that. As a part of this research study, the angular dependence of MR in nanocrystalline Ni and Ni-Fe alloys was reported. MR of these materials and, the contribution of the magnitude of the applied field and sample orientation are also taken into account in this research study.

2.5. Electrodeposition of Ni and Ni-Fe Alloys

Among various production techniques, electrodeposition offers flexibility, low cost, as well as size and geometry independent output and therefore represents an advantageous method for producing Ni-Fe alloys [71]. Electrochemical production technique is possible via direct current (DC) plating, pulse plating, and CO-deposition [72,73,74,75]. Nanostructured Ni-Fe alloys made by electrodeposition have reported to have high strength, increased wear resistance as well as excellent soft magnetic properties without modifying the coefficient of thermal expansion [1]. This technique employs rather inexpensive equipment and can be performed under normal conditions of temperature and pressure [76]. To date, the extensive research on electrodeposition of various alloys have resulted in the fact that by varying the deposition parameters and the electrolyte composition, the microstructure, composition and the grain size of the deposits can be tailored. Therefore by tailoring these factors, aside from processing variables such as bath chemistry, pH, temperature, the applied current density and electrolyte mixing conditions, consequently parameters such as roughness, grain size, and alloy composition are changed. Such changes finally result in different magnetic, mechanical, and corrosion properties of Ni-Fe electrodeposits. Any changes in these variables may lead to non-uniformities in the composition of the electrodeposited structure. Two competitive actions of building up of existing crystals or forming new ones are the two dominant phenomena in electrodeposition. These two phenomena are under influence of the two key mechanisms of charge transfer at the electrode surface and surface diffusion of ad-ions on the crystal surface. When the condition is set the way the overpotential is high and diffusion rates are low, the tendency to form nuclei is increased while in the opposite condition grain growth is favoured.

2.5.1 Ni Electrodeposition

The electrodeposition of Nickel dates back to 1837 and the research on improving the properties of the deposited layers is still ongoing. The effect of different baths, pH values, current densities and temperatures on various substrates has been examined [77, 78]. The vastly accepted deposition mechanism for Ni is a two-step, electron charge transfer mechanism, in which the cationic Ni-complex is absorbed by the substrate [79]:

$$Ni^{2+} + X^{-} \leftrightarrow NiX^{+}$$

$$NiX^{+} + e^{-} \leftrightarrow NiX_{ads} \qquad (2.26)$$

$$NiX_{ads} + e^{-} \leftrightarrow Ni + X^{-}$$

The anion X^{-} was assumed to be OH^{-}, SO_4^{2-} or Cl^{-} [79].

2.5.2 Models for Ni-Fe Alloy Electrodeposition

Alloy deposition consists of instantaneous deposition of two metals, which leads to finer grains and a harder, stronger, and more corrosion resistant structure than the parent metals with high magnetic permeability. An important parameter is to control the electrolytic bath during the deposition. The special and various properties of Ni-Fe alloys such as high strength, hardness and magnetic properties have made the electrodeposition of these alloys to be subject of extensive research [80, 81, 82, 83,84,85,86].

There are various types of Ni-Fe alloys which are magnetically isotropic. These alloys cover a wide range of Fe content with different applications: from Ni-20% Fe (Permalloy) with excellent magnetic properties (maximum permeability and a high coercivity) for magnetic applications to Ni-50%Fe with only decorative applications. Based on previous studies, the magnetic properties depend on the thickness of the deposited film (best between 500- 5000Å), composition, roughness of the substrate, and crystallite size as well as the internal stress in the deposit layer [87,88,89].

Electrodeposition of Ni-Fe alloys offers the advantageous anomalous co-deposition phenomena initially seen by Bernner, in which, the reduction of nickel is inhibited while the deposition of iron is enhanced. In other words, anomalous co-deposition, is the effect where in the binary alloys of two iron group metals (iron, cobalt, and nickel), the less noble metal deposits for a wide range of deposition conditions, which leads to a larger concentration of the less noble metal in the film than in the solution [80]. It has been proved that by changing the $Ni^{2+/}Fe^{2+}$ mass ratio in the electrolyte, Ni-Fe alloys with iron contents in the range from 7 to 31% can be obtained. Increasing this ratio leads to increasing the iron content in the bath and consequently in the deposits [90]. In recent years, several models have been developed to explain this behaviour, one of which was introduced by Dahms and Croll, in 1960. They claimed that the corresponding metal reduction reactions occur in the anomalous co-deposition described by the following equation [91]:

$M^{2+} + OH^{-} = MOH^{+}$,

$MOH^{+} + e = MOH_{ad}$,

$MOH_{ad} + e = MOH^{-}$.

Where M can be either Ni or Fe.

In this condition, if the pH is large enough, ferrous hydroxide is formed and leads to blocking of Nickel deposition as its being absorbed by the electrode surface.

A mathematical model including the mass transfer equations and the interfacial kinetics in order to assess the surface pH, the formation of metal-hydroxide ions, and the concentration of the metal ions at the surface (solved numerically) was then presented by Hessami and Tobias [92]. They explained that in the same pH, the dissociation constant of $FeOH^+$ is smaller than that of $NiOH^+$, which results in more discharge of $FeOH_{ad}$ on the cathodic surface than nickel ions. Accordingly, increasing the bath pH always leads to production of more $Fe(OH)_2$, and consequently increase the iron content of the alloy film. The trend observed for variating the temperature is the opposite way around [93]. Later on, it was confirmed by Matlosz that the reduction of nickel and iron are two-step reactions, and inhibition of nickel at a specific potential is not pH dependant and is mainly due to preferential surface coverage of the adsorbed iron [94]. A study on deposition of Ni-Fe alloy from a sulphate bath reported that Ni^{2+} and Fe^{2+} electroactive species and that hydroxide species are not the ones responsible for the deposition mechanism. In 2004, Plieth and Georgiev proposed a theory called *the finite Markov chain theory*, which defines the relationship between the alloy composition and the corresponding metal ion concentrations in the electrolyte as well as the residence time of components of the alloy in the kink site positions of the surface [95]. It has been reported that the electrolyte composition affects the grain size and composition. The research done by Li and Ebrahimi indicated that increasing the Ni/Fe ratio of the electrolyte leads to a lower-Fe content alloy with a larger grain size [96]. The authors also stated that the process of electrodepositing nickel and iron and nickel-iron alloys are dominated by diffusion with a typical three-dimensional nucleation and growth mechanism.

In terms of mechanical properties, it has been found that by lowering the $Ni^{2+/}Fe^{2+}$ mass ratio (or increasing current density), therefore increasing the iron content, higher microhardness can be achieved. This effect has been attributed to the reduction of the grain size and a more crystallographically orientation referred structure [97, 98].

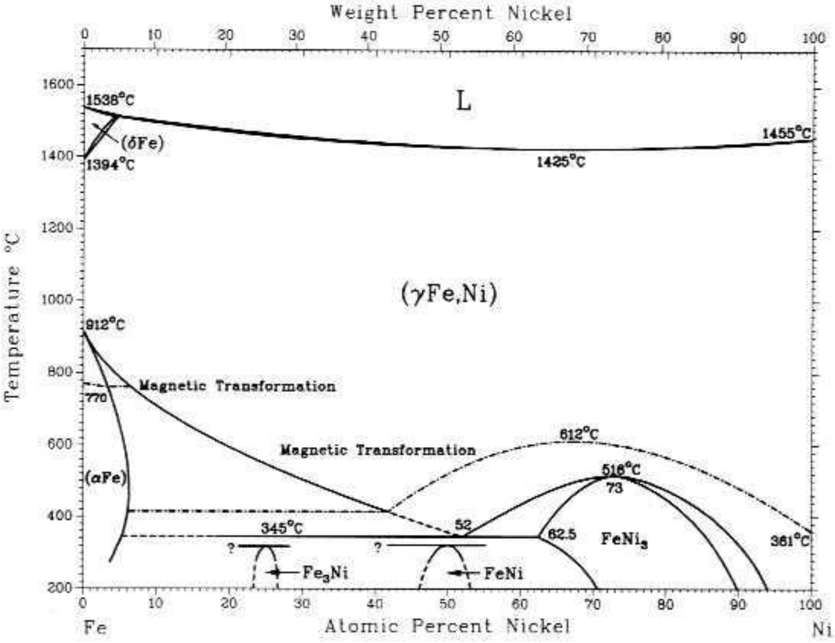

Figure 2.9 Phase diagram of Ni-Fe alloy [99].

According to Abdel-Karim et al.(2011), for a long range of $Ni^{2+/}Fe^{2+}$ mass ratio of the bath, the dominant phases in electrodeposited nanocrystalline (20–30 (nm)) Fe-Ni alloys are either Ni-based solid solutions or Ni_3Fe phase. Increasing the iron content leads directly to higher Ni_3Fe phase deposit [100]. Ni_3Fe structure is a cubic crystal embedding three Ni atoms each at the center of the cubic face and a Fe atom at the corners of the cube. Ni and Fe are completely soluble in each other; however, at compositions nearing Ni-25%Fe (Ni_3Fe) and Ni-75%Fe (Ni_3Fe) ordering tendencies have been observed. Figure 2.9 illustrates the phase diagram of Ni-Fe [101]. The crystal structure of nickel-rich iron alloys is FCC while the iron-rich is BCC [96].

In terms of texture, it has been found that nanocrystalline Ni-20%Fe (PERMALLOY) alloys exhibit weaker texture than the ones formed in coarse-grained structures. This phenomenon has been explained by a general trend that the increased cathodic current density at the deposition is more or less the same as the quenching effect on a molten alloy. In fact, having higher cathodic current density during electrodeposition means ions with high excess energies. When these ions reach the cathodic surface, they do not have enough time to find the most suitable position in the lattice and therefore randomly oriented grains with high density of structural defects are created [102].

Reduction in any of the texture components is a good indication of increasing volume fraction of grains with random orientation.

2.5.3 Development in Nanocrystalline Ni-Fe Alloys

Conventional γ-Ni-xFe alloys with x being in the range of 10% – 65 wt%, have been used in industry for years due to their excellent soft magnetic proprties [103]. The γ-Ni-22%Fe alloy called Permalloy with high permeability, low coercivity and relatively high saturation magnetization is the most well-known of these alloys. Many applications of soft magnetic materials involve high saturation magnetization. Due to the fact that Fe is a stronger ferromagnet than Ni, it is expected that by increasing the iron content in the Ni-Fe system, it would meet the requirement of a perfect soft magnetic material. On the contrary, increasing the Fe content of the Ni alloys, leads to both an increase in the coercive force and a decrease in permeability due to the increase of the magnetocrystalline anisotropy. Consequently, the performance of the material as a soft magnetic material deteriorates. From the grain size improvements, it has been also realized that nanoprocessing can effectively reduce the magnetocrystalline anisotropy constant of a material (when $D < L_{ex}$) and enhance the coercivity and permeability of the material. A study was conducted on mechano-chemically synthesized γNi-xFe alloys with x =32, 46, 55, and 64wt% and grain sizes in the range of 30–40 (nm) [104]. It was found that H_C of sample (with the lowest iron content) was substantially smaller than that of the other samples at all the temperatures indicating magnetocrystalline anisotropy was the dominant factor (see Figure 2.10) [104]. Microstructural analysis indicated that relative high coercivity for the nano γ-Ni-Fe alloy with higher iron content (x = 64wt %) was mainly caused by its larger shape anisotropy. In terms of saturation magnetization, it was found that the variation of the saturation magnetization of nano γ-Ni-xFe alloy with iron content is similar to that of its polycrystalline counterpart and it rises with increasing the iron content [104].

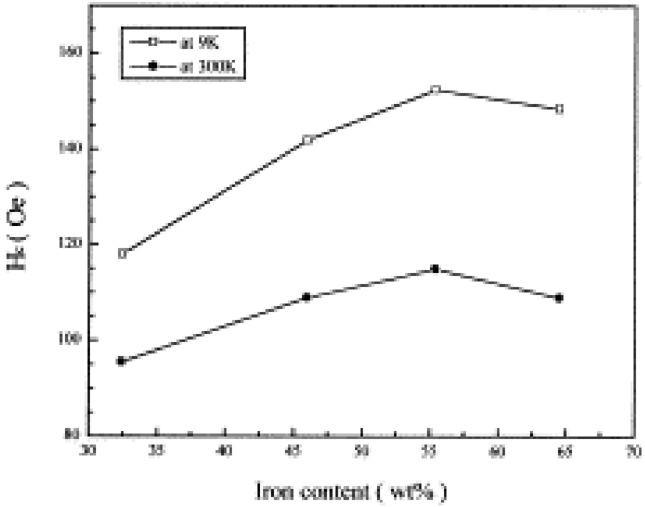

Figure 2.10 Plot of coercivity (at 9K and RT) of nano-γ-Ni-xFe versus iron concentration.

The as-deposited microstructure of electrodeposited nanocrystalline Ni–Fe alloys has been studied by several researchers by the application of transmission electron microscopy (TEM) [104, 105, 106, 96, 107] scanning electron microscopy (SEM) [105, 106, 107] X-ray diffraction (XRD) [106, 96, 113] and atomic force microscopy (AFM) [113]. These studies have led to characterization of the following microstructural parameters: mean grain size [96, 106, 113, 113, 108, 109], grain size distribution [96, 105, 109], and crystallographic texture [96, 105, 106, 110].

The first experimental verification of the random anisotropy model (RAM) on nanocrystalline Ni and Ni-Fe alloys was conducted by Beke in 1996. Although his prediction for the relationship between the coercivity and the grain size was not accurate;

however, he successfully showed the concentration dependence in saturation magnetization of Ni and Ni-Fe alloys (with a ratio of 1.46) [111].

The research study undertaken by Cheung et al. in 2002 on electrodeposition of Ni and Ni-Fe with varying iron content up to 22%, has resulted in an increase in saturation magnetization from 0.6T to 1.02T, respectively. In terms of coercivity, it was proved that these alloys follow the D^6 relationship predicted by Herzer [112]. XRD patterns of the Ni-Fe alloys showed that crystallographic texture shifts from an initial (111)/(200) double fibre texture to a stronger <111> component as the Fe content increases to 22%. Also it was found that the grain size decreases from 21 (nm) (Ni-0 wt % Fe) to 11(nm) (27.9 wt % Fe). This study suggested that low coercivity can be obtained by grain size reduction, regardless of the synthesis route. Another study was conducted by Czerwinski, Szpunar and Erb in 2001, on nanocrystalline Ni-20%Fe Permalloy resulted in deposits with γ phase with a grain size of 10± 15 (nm) and a strong <100> fibre texture with some contribution of the <111> component [113]. A recent investigation of dynamic magnetization reversal process in electrodeposited nanocrystalline Ni and $Ni_{80}Fe_{20}$ films resulted in nanostructures with grain sizes of 102.4 (nm) for both Ni and $Ni_{80}Fe_{20}$ films and coercivity values of 20 and 14 Ka/m^{-1}, respectively. The surface texture of these samples showed deposits consisting of columnar grains that contributed to magnetic anisotropy and higher coercivity [114].

Chapter 3

Experimental Procedures

Introduction

A brief introduction of the experimental techniques used for the characterisation of nanocrystalline Ni and Ni-15%Fe alloys is presented in this Chapter. Complementary structural and magnetic investigation techniques that were employed in this research study are also discussed. The main intent of this Chapter is to discuss experimental approaches used to investigate the effect of composition and temperature on the texture and magnetic properties of the prepared samples.

3.1. Nanocrystalline Samples

Electrodeposited nanocrystalline Ni and Ni-15%Fe with the thickness in the range 50 μm -250 μm were received from Integran Technologies Inc. Toronto. The average grain size of the samples was obtained by Dr. Gordana Cingara under TEM diffracting conditions. The grain size of Ni and Ni-15%Fe samples were about 23 and 12 (nm) respectively.

3.2 Characterization Techniques

3.2.1 X-ray Diffraction (XRD)

Among all characterization techniques, X-ray diffraction (XRD) has the advantage of being a non-destructive method used to characterize the crystallographic structure and the preferred orientation in a sample. The X-Ray Diffractometer instrument is composed of an a X-rays source (a X-ray tube, for example), an X-ray detector and a goniometer, which provides precise mechanical motions of the tube, sample and detector, and the electronics for counting detector pulses in synchronization with the positions of the goniometer [115]. This technique, mainly functions according to the Bragg's condition: Crystallinity of the samples is confirmed when a set of atomic planes of the sample parallel to the substrate, satisfies the Bragg's condition. In this case, in the X-ray diffraction pattern, distinct peaks are observed. In addition to crystallinity, texture of the sample can be examined by XRD. If the sample is textured, preferential reflections from a certain family of atomic planes parallel to the substrate surface, so called {hkl} are exhibited.

Phase identification is also possible via comparing the designated d-spacing of these planes with the powder diffraction file (PDF) database. Since in the Bragg-Brentano geometry, only lattice planes parallel to the sample surface are present in the XRD patterns, for textured samples only few families of reflections are observed.

Structural analysis of the deposits were done on Ni and Ni-15% Fe samples at room temperature with Brukers Smart6000-D8 Diffractometer with parallel-focused CuK_{α} (λ = 0.154 (nm)) radiation. In order to improve the accuracy of the measurements three different scans were done on the samples with detector-sample distance of 16.72 mm. The scans were done at $2\theta = 36^{o}$, $\omega = 198^{o,}$ $2\theta = 60^{o}$, $\omega = 210^{o,}$ and $2\theta = 84^{o}$, $\omega = 222^{o}$, respectively with scanning time of 300 seconds. The three frames recorded from experiments were further combined using the software MERGE and the transferred to TOPAS software for structural determination. Here in, rings observed in the diffraction patterns proved texture in samples. In order to get refined information on the crystal structure of the studied materials, their X-ray powder diffraction patterns were analyzed by means of Rietveld refinement [116]. This method is a powerful tool for the extraction and refinement of structural information from Powder diffraction patterns, quantitative phase analysis, and obtaining microstructural characteristics such as crystallite size. The refinement involved minimizing the differences between a calculated pattern based on a starting structure and the experimental diffraction pattern by adjusting iteratively the crystallographic and instrumental parameters affecting the intensity at each diffraction angle. The least squares structure refinement of the investigated alloys X-ray powder diffraction was done using the computer program 'Topas"[117].

The microstructural characteristics including the cell parameter and crystal density were obtained from this analysis. The decency of the least-squares structure refinement can be assessed by Rwp factor, which is the most significant indicator of the agreement between the crystal structure model calculated intensities and the actual structure (observed intensities).

3.2.2 Pole Figure Analysis

A useful technique to determine the orientation relationship of the film as well as to identify the phase identification of the sample is measuring the pole figures. Orientation Distribution Function (ODF) of a set of planes can be achieved by setting the diffraction condition ($\theta - 2\theta$) to the corresponding lattice spacing, defined by Bragg's equation, while rotating (ϕ) and tilting (ψ) the sample, in the mean while recording the intensity at these different orientations. Poles are generally illustrated by their Miller indices (hkl), the same manner the crystallographic planes and are the projection of the normal of a plane onto a 3-D sphere residing around the circle. The presence of the distinct pole is indication of not only the out-of-plane texture but also an in-plane texture which is mostly due to electrodeposition conditions or buffer/substrate direction known as epitaxial relation. Existence of rings in each pole figure shows that the crystallites are oriented along a certain crystallographic axis.

Ni and Ni-Fe pole figures ($0 \leq \varphi \leq 360°$ and ($0 \leq \psi \leq 82°$) have been measured with a Brukers Smart6000-D8 Diffractometer with parallel-focused CuK_α (λ = 0.154 (nm)) radiation (Rigaku RU-200-rotating anode, 50kV/90mA). Before starting the pole figure measurements for a certain reflection, the ($\theta - 2\theta$) value was set on an expected pole for maximum intensity. Then the samples were measured at fixed 2θ values. The Pole figures and the ODF projections were and created using GAADS 4.1.29 and Multex 3 software.

3.3 Magnetic Measurements

Magnetic properties of Ni and Ni-Fe samples were studied using a commercial Quantum Design PPMS-9 system. The experiments were designed to measure the component of the vector of the net magnetization parallel and perpendicular to the applied magnetic fields. DC magnetization studies were performed using the extraction magnetometer option. The temperature dependence of DC magnetization was studied by measuring hysteresis loops in the field ranges between -4 (Tesla) ≤ H ≤+4 (Tesla) at temperatures 2K and 298K. The external magnetic field was changed in the sweep mode at a sweep rate of 10 (Oe/ min). Complete hysteresis loops were recorded while sweeping the fields from positive to negative saturation and vice versa.

3.4 Magnetoresistance measurements

Magnetoresistance (MR) measurements were performed on nanocrystalline Ni and Ni-15% Fe samples with a standard four-probe configuration using a physical property measurement system (PPMS-9) which was equipped with a sample rotator at a temperature of 2K. The samples of dimension 0.2 mm x 1mm x15mm were mounted on a platform of rotator, the potential and current leads were spot welded to the samples using laboratory welder. The samples were rotated in the constant magnetic field of 9 (Tesla) every 2 degrees and the resistance of the samples was measured by averaging 25 pairs of potential measurements. This way, the transverse MR data in which, the electrical current (I) and external field (H) are perpendicular to each other at any measurements point, were collected. The minimum and the maximum values of the resistance ($\rho\|$ and $\rho\perp$) were obtained in saturated fields of 9 (Tesla).

In this research study, the MR is defined as:

$$\mathrm{MR} = \frac{\rho-\rho_{\perp}}{\rho_{\perp}}\times 100 \tag{3.1}$$

Where $\rho_{\perp}$ is the maximum resistivity value when the sample is perpendicular to the magnetic field at applied field of 9 (Tesla).

The resistivity as a function of magnetic field was also measured at temperature of 2K, by scanning the field range from 0 to 9 (Tesla).

Chapter 4

Results and Discussion

Introduction

In this Chapter, texture, and magnetic properties of nanocrystalline Ni and Ni-Fe alloys and their dependence on temperature, composition, and magnetic fields are studied. In the following Section (4.3.3), the random anisotropy model (RAM) on the materials studied is presented followed by a discussion on the parameters affecting its validation. In the last Section of this Chapter, an investigation on the angular and field-dependence anisotropic magnetoresistance (MR) of nanocrystalline Ni and Ni-15%Fe samples is presented. A discussion on the origin of soft magnetic behaviour of these nanocrystalline alloys in terms of magnetizing process on the basis of MR and RAM concludes this research study.

4.1 Structural Determination and Texture Analysis

4.1.1 Structural Determination

The nanocrystalline Ni and Ni-15%Fe materials were fully dense in bulk form with a thickness of about 50 (μm). The three frames recorded in XRD experiments were combined using the software MERGE and were transferred to TOPAS software for structural determination. The X-ray powder diffraction patterns were analyzed by means of Rietveld refinement. The studies of the internal stress were beyond the scope of the present research project.

Figure 4.1 illustrates the profile fit and the diffraction patterns for nanocrystalline Ni and Ni-15% Fe samples respectively. As apparent from Figure 4.1, the calculated pattern (red lines) fits the observed (Ni: black and Ni-15%Fe: blue) ones very well. The crystal structure of Ni-rich alloys is expected to be FCC as denoted by many research studies [108, 114]. As expected, peaks are indexed to a FCC structure with space group of Fm3m. The Thompson-Cox Hastings Pseudo-Voigt function was used in Topas software for the representation of individual reflection profiles. The refined parameters were: background parameters, sample displacement, 2θ zero-point, lattice constants, profile half-width parameters (u, v, w), the mixing parameters of the Pseudo-Voigt function (NA, NB), asymmetry correction factor (P), occupation factors, atom coordinates (x, y, z), and isotropic thermal parameters. The Rietveld fits yield satisfactory crystal structure with values of Rwp-factors for Ni and Ni-15%Fe of 1.709 and 1.710 respectively. These values were found to be extremely sensitive to the reflection profile functions used to describe the observed diffraction line profile.

In Figure 4.1, the most intense peak of Ni at 2θ = 44.49° is attributed to the (111). The rest of the legible major peaks are marked as the (200) and (220) planes peaks with respect to the intensity at 2θ = 51.84° and 76.37°, respectively. The indexed peaks and the achieved 2θs are in agreement with previous research studies [118,119, and 120].

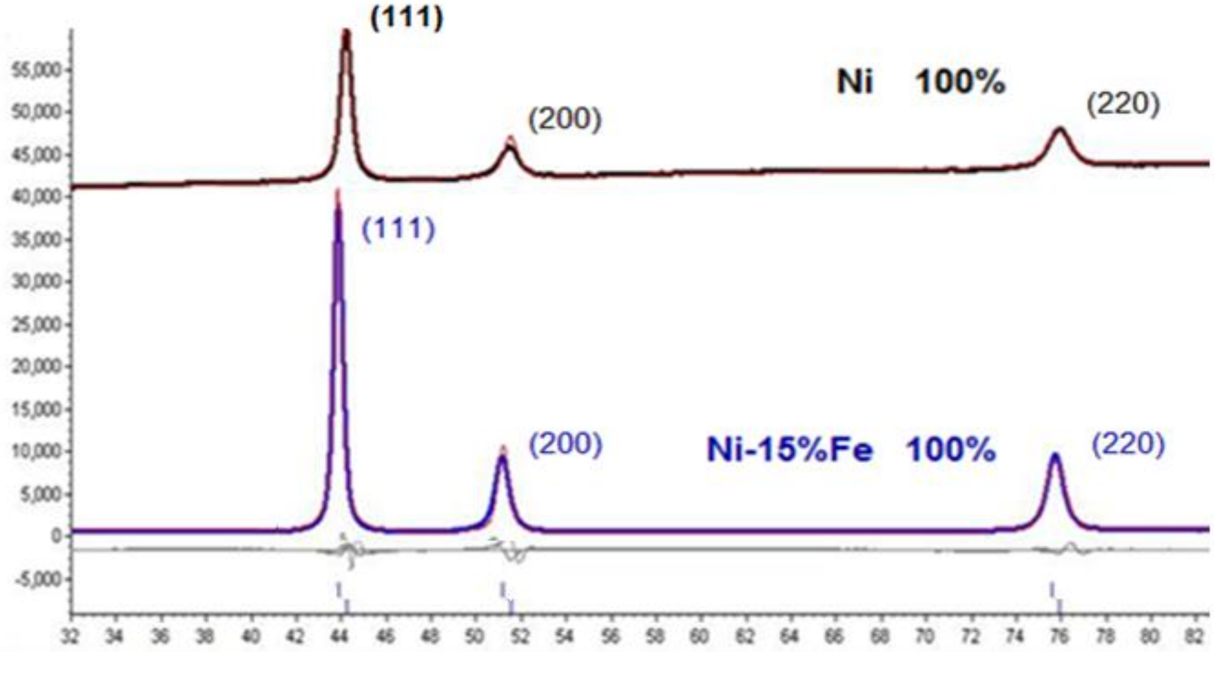

Figure 4.1 The XRD pattern of experimental black: Ni and blue: Ni-15%Fe. The red patterns correspond to the calculated patterns.

The Ni-15% Fe alloys obtained under the conditions of this study [96, 101] are composed entirely of γ phase, which is a solid solution of Fe in Ni, in which the Fe solutes are replaced in the Ni sites in lattice The shift in the angular location of diffraction peaks in Ni-15% Fe alloy in comparison to the JCPDS standard for nickel is evident from this phenomenon.

In the diffraction pattern of nanocrystalline Ni-15% Fe sample, three peaks can be observed for the range of 2θ angles from 30° to 80° corresponding to a cubic FCC Ni-Fe structure (space group 225-Fm3m), which describes the Ni-Fe alloys with compositions from 100% Ni to 24.81%Ni). The most intense peak located at 2θ = 43.91° is again attributed to the (111) plane. The second and the third peaks are similarly marked as the (200) and (220) planes peaks at 2θ = 51.02° and 75.25° respectively in agreement with the previous studies on nanocrystalline Permalloy system [113]. Two observations are worth mentioning with regards to the diffraction patterns. First is the position of peaks and second is the broadening of the peaks in comparison with the standard data. It can be clearly observed that the positions of the peaks in the case of Ni-15% Fe samples are shifted to lower 2θ values. Returning to the Bragg equation: $n\lambda = 2d\sin\theta$ and by considering the CuK_α wavelength, the results provide evidence of changes in interatomic spacing and that the d spacing of the corresponding planes in Ni-15% Fe is larger than that of Ni sample, which means that unit cell parameters of this sample is larger than unit cell parameters of pure nanocrystalline Ni sample.

The unit cell dimensions of Ni and Ni-15%Fe were refined to be a = b =c= 3.5270 ± 0.0009Å, and a = b = c= 3.5424 ± 0.0021Å, respectively, which are consistent with literature values [104]. The increase in the lattice parameters with increasing the iron content of the nanocrystalline Ni deposits found in this study is consistent with the behavior observed in electrodeposited FCC Ni-Fe alloys. On the other hand, the values measured in this study are slightly lower than those reported in the literature. This may be due to the development of residual lattice strains in the deposits or the existence of the compressive stresses along the crystallographic directions whose peaks were used to calculate the lattice parameter [121].

The second observation is related to the broadening of the diffraction peaks that are much broader than the single crystal diffraction pattern available on the data base. It is known that the broadening of the diffraction peak is proportional to the size of the crystals. Any decrease in either grain size or lattice strain will cause effective broadening of the diffracted peaks, and if the crystal size is less than 1000Å, peaks appear broader on diffraction pattern than corresponding peaks of a single crystal. Also the change in peak intensities, as compared to the standard, is apparently due to the presence of the preferred orientation. In order to determine the crystallographic texture, the pole figures were measured with an X-ray goniometer, which were subsequently used as a basis to calculate the orientation distribution functions.

It should also be emphasized that the ratio I(200)/ I(111) of the intensities of (200) and (111) peaks for random orientation is about 0.42 for Ni. In contrast, the value of I(200)/ I(111) for nanocrystalline Ni and Ni-15% Fe samples are about 0.75 and 0.27, respectively. This ratio value indicates that the X-ray diffraction patterns of both samples are not random. This is indirect evidence of texture in both samples.

4.1.2 Texture Analysis

In texture analysis, the preferred orientations and directions of the texture components were first estimated interactively and then calculated numerically by least squares fit together with the other component or pole figure parameters. Alternatively, one component or several components are fitted. To quantitatively analyze the texture of the samples, three incomplete pole figures, {111}, {200}, {220}, were measured in the range of the polar angle α from 0° to 82° with Co Kα radiation. ODFs were calculated from the measured pole figures using Multex 3 program. ODF, is a complete description of texture which consists of isointensity contour plot of various crystal orientations with respect to the sample reference frame and is illustrated in the Euler angle space [122]. Analysis of ODFs yields quantitative texture data on the volume fraction of texture components. In Multex 3 program, a geometric approximation method for the texture calculation from diffraction pole figures is used. The reduction of the texture data to a few components allows pole figure-based texture estimations. With the construction of ODFs and performing component fit, a full range of φ angles were obtained on the pole figures. The component fit is performed directly in pole figure space and it relates maxima in pole figures directly to preferred orientations and is therefore easy to visualize.

Figure 4.2 illustrates the {111}, {200}, and {220} pole figures for the textures of nanocrystalline Ni sample. The first column contains the experimental pole figures, the second one: the recalculated pole figures from ODF analysis and the last column contains the difference between these two. Ni sample shows fibre texture with a major component of the <100> axis, aligned perpendicular to the specimen surface. There exist a second major component of <111> fibre which has a considerably lower strength. Since in a FCC structure the angle between (200) and (111) planes are about 54°, a ring within the (111) pole figure is expected in agreement with the experiments. As the angle between two neighbouring (100) planes is 90°, they are not evident in the (200) pole figures. Similarly, the central (111) reflection can be explained. The angle between two (111) reflections is 70° denoted the existence of a broad ring in the (111) pole figure. Arguments above confirms the existence of a ring at ≃51° in the (200) pole figures, which cannot be observed significantly due to much lower intensity of the (200) planes compared to (111) planes. The volume fraction of the two fibre components of <100> and <111> are calculated by means of Multex 3 software and are 22.032% and 6.160%, respectively and the rest is random texture. The Vol% is reported relative to the total scattering, including background, etc., depending on how the system is defined.

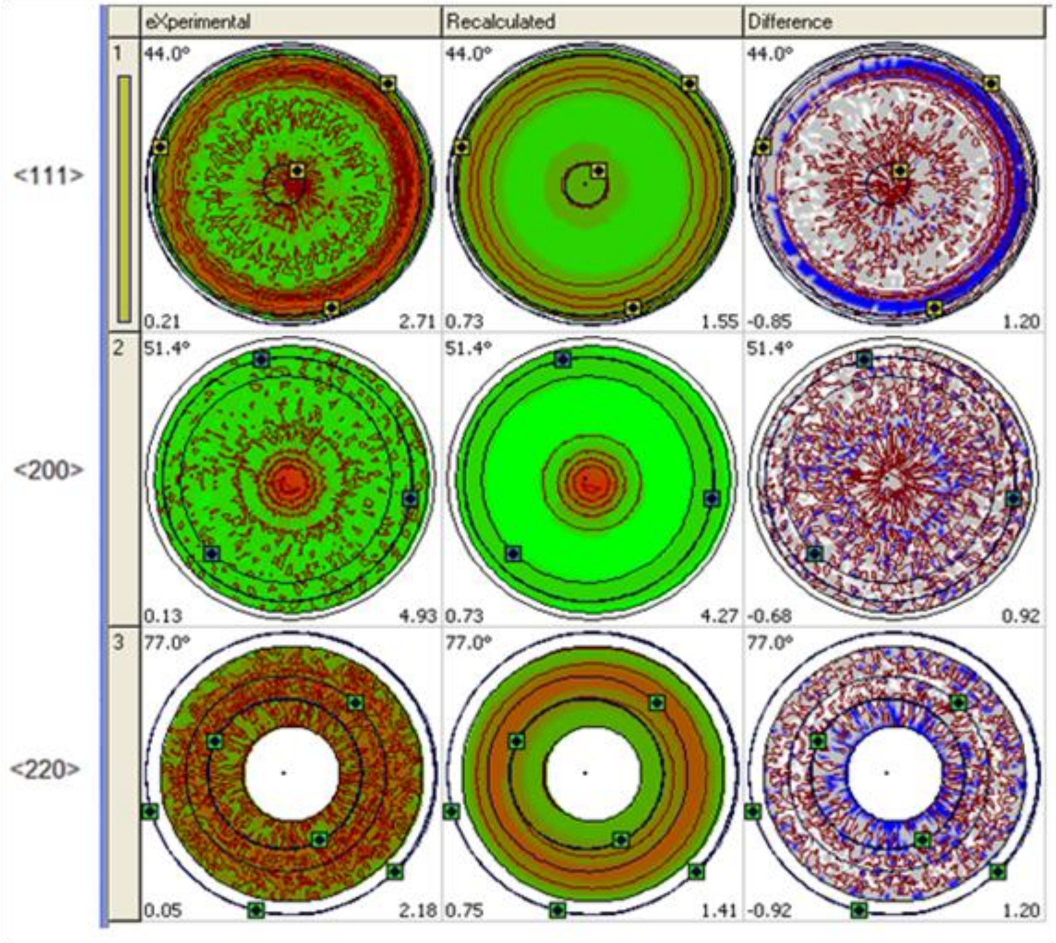

Figure 4.2 Completed <111>, <200>, and <220> Pole figures of nanocrystalline Ni sample (a) experimental pole figures (b) the recalculated pole figures and (c) the difference map of experimental and recalculated pole figures.

Figure 4.3 shows the fibre texture of the Ni-15% Fe sample. As apparent from the Figure, the calculated pole figures of this sample also confirms a fibre texture with a major component of the <100> axis, and a second major component of <111> fibre. The overall randomness of the texture in nanocrystalline Ni-15% Fe sample is higher than the Ni sample. The calculated volume fraction of the <100> and <111> components are 17.157 % and 3.201%, respectively and the rest is confined to random texture. Table 4.1 summarises the microstructural observations of texture of two samples.

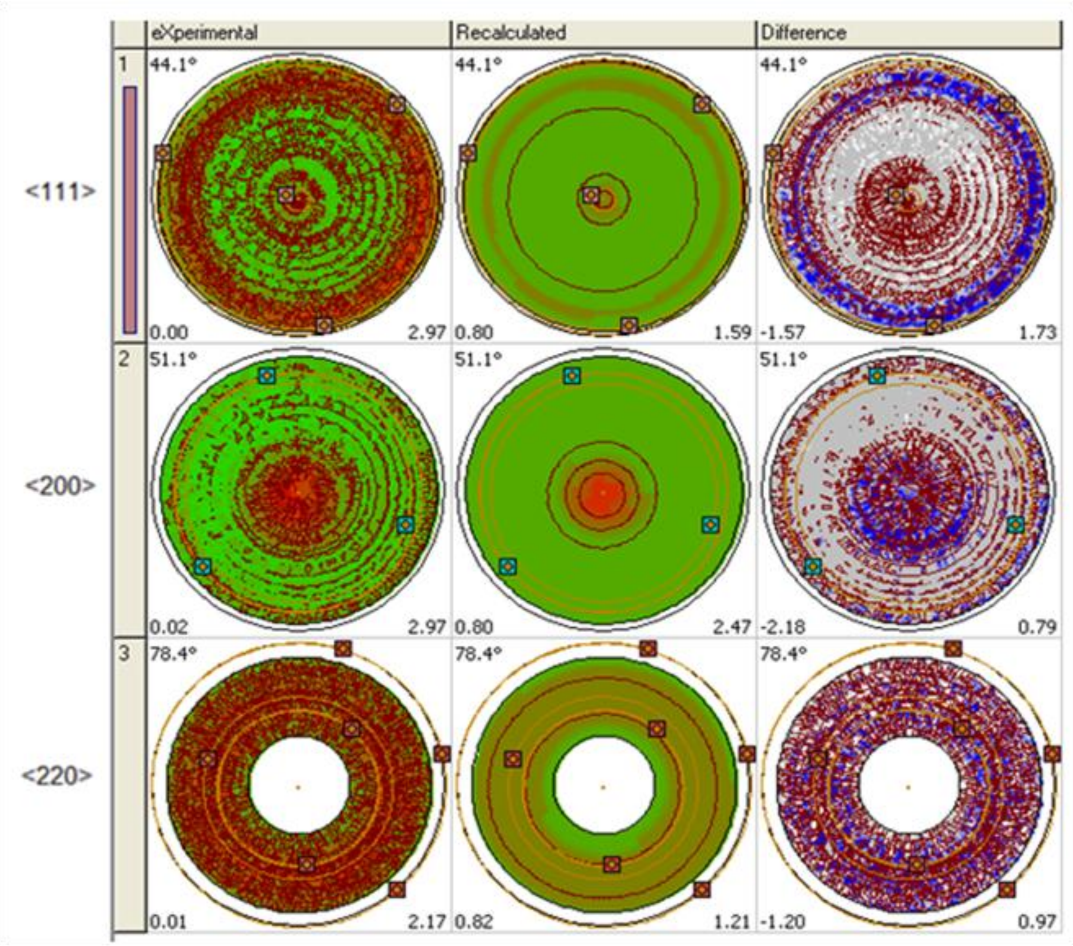

Figure 4.3 Completed <111>, <200>, and <220> Pole figures of nanocrystalline Ni sample (a) experimental pole figures, (b) the recalculated pole figures and (c) The difference map of experimental and recalculated pole figures.

In Ni-15%Fe Pole figures, broader rings between Ψ = 44.1° and 78.4° are observed in addition to the central peaks. This confirms more randomness in the texture.

As mentioned in Chapter 3.1, that the grain size of the Ni and Ni-15%Fe samples were determined to be 23 and 12 (nm) respectively. This data was further used to confirm the observed texture. It was previously discussed in Section 2.5.2 that increasing iron content in the Ni alloys leads to smaller grain size. Based on prior studies, the bigger the grain size, the stronger texture in the material. This is due to the fact that the intensity of the diffractions from crystalline plane is strongest in case of single crystals. Consequently, Single crystalline materials exhibit much stronger fibre texture than poly and nanocrystalline materials. As for the Ni, it has been seen that smaller crystallites lead to a weaker texture [105]. 15% of Fe content in Ni-15%Fe sample did not cause any change in alloy phase composition beyond the FCC structure. Therefore the structure remains the same, but due to fabrication process, and inhibiting behaviour of iron atoms from the electrolyte while electrodepositing, Ni-15%Fe sample attained smaller grain sizes. Therefore the weaker texture in the nanocrystalline Ni rather than Ni-15%Fe can be attributed to the smaller grain size of the materials.

Ni and Ni-15%Fe exhibit a fibre texture with major component of the <100> axis. A second component of <111> also exists with a significantly lower strength. Nanocrystalline Ni sample shows 71.808% of random orientation whereas Ni-15% Fe shows 79.642 % random orientation. Table 4.1 presents a summary texture data for two samples of nanocrystalline Ni and Ni-15% Fe samples including the volume fraction of texture components in the samples and their corresponding b values. It should be mentioned that the b value is a quantitative measure (refined) of the orientation distribution of the poles about the refined direction. It is like a FWHM value of the Gaussian distribution about the component vector.

Table 4.1 Summary of texture components, their volume percent and their broadening of nanocrystalline Ni and Ni-15%Fe alloys.

Sample	Major Texture component	Volume %	b
Ni	100	22.032	18.54
	111	6.160	19.42
Ni-15% Fe	100	17.157	24.00
	111	3.201	9.59

4.2 Magnetic Properties

This Section elaborates on the effect of composition, temperature and the direction of the magnetic field on the magnetic properties of nanocrystalline Ni and Ni-15%Fe bulk alloys. Magnetic measurements were carried out at two temperatures of T=2K and 298K (room temperature) using the standard methods. Dependence of magnetic properties on various micro structural parameters is presented with the aim to provide a better understanding of the various mechanisms to determine the soft magnetic behaviour of these materials. Magnetization data are result of high field extrapolation of the isotherms recorded in DC-magnetization measurements up to +4 (Tesla). The magnetization versus applied field (M-H) curve gives important information on the magnetization process. It was employed to provides important magnetic parameters such as: saturation magnetization (M_S), susceptibility (χ), coercivity (H_C) as well as the permeability (μ). How the magnetization of a material changes at different temperatures also provides useful information on the magnetic structure. These experiments have been conducted using Quantum Design Physical Properties Measurement System (PPMS) with a 9 (Tesla) superconducting electromagnet cooled with liquid helium.

4.2.1 Temperature Dependence of Magnetization

MH-Dependence at T = 2K

Magnetic properties were determined at two different temperatures of T=2K and 298K by applying a magnetic field up to 4 (Tesla) both parallel (φ = 0°) and perpendicular (φ = 90°) to the sample plane. The Hysteresis-loops along the x and y axes of the nanocrystalline Ni and Ni-15% Fe sample measured at T=2K are depicted in Figure 4.4. It should be noted that they have not been corrected for the demagnetization field contribution. Each hysteresis loop is identical along both negative and positive applied magnetic field values. This indicates that the net magnetic properties are isotropic in the direction of the bulk samples. The hysteresis loops for the two orientations of the field with respect to the film plane have different shapes, which indicate the presence of an in-plane magnetic anisotropy.

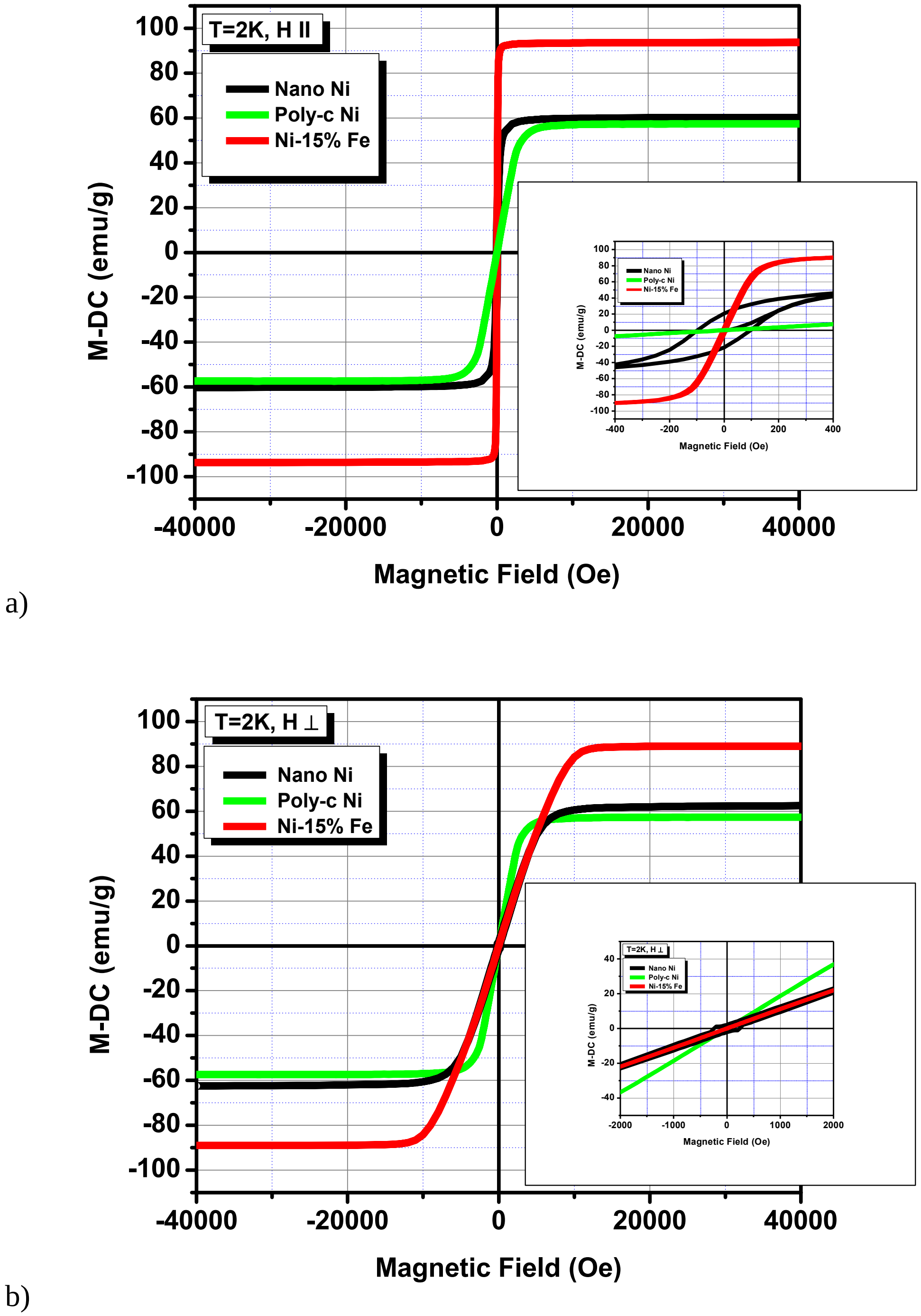

Figure 4.4 Hysteresis loops of polycrystalline Ni, nanocrystalline Ni and Ni-15% Fe samples where the magnetic fields up to 4 (Tesla) were applied a) parallel ($\varphi = 0°$) and b) perpendicular ($\varphi = 90°$) to the sample plane at T=2K.

First observations on the hysteresis loops is that in both Figures, nanocrystalline Ni and Ni 15%Fe samples possess narrow hysteresis loops which denote low losses and soft magnetic behaviour. In case where the field is applied parallel to the sample plane; the saturation Magnetization of the sample containing 15% Fe is about 93.67 (emu/gr), which is 33.501 (emu/gr) higher than that of nanocrystalline Ni (60.169 (emu/gr)). This arises from the larger atomic magnetic moment of iron than that of nickel, which increases the magnetization.

It is known that the saturation magnetization is compositional-dependant and not structural-dependent. Therefore, it is expected that the saturation magnetization of the polycrystalline Ni do not vary much from that of nanocrystalline Ni. The saturation magnetization of these two materials are 57.352 (emu/gr) and 62.436 (emu/gr) respectively for Poly and nanocrystalline Ni samples.

It is apparent from the Figures that the permeability of both Ni and Ni-15%Fe samples when the field is applied parallel to the sample plane is higher than in the perpendicular case. This effect can be attributed to the size effect and the magnetocrystalline anisotropy of the samples. Size effect occurs in thin samples and is illustrated in Figure 4.5.When the applied field is oriented parallel to the sample plane, the action of magnetic moments aligning toward the magnetic field requires less energy and this results in easy and fast rotation of magnetic moments toward the field and reaching saturation in fields less than 1000 (Oe) (see Figure 4.5). However, when the field is applied perpendicular to the plane of the sample, a significantly higher field is required to saturate the magnetization and saturation takes place in fields up to 10000 (Oe). The effect of magnetocrystalline anisotropy on permeability is discussed further.

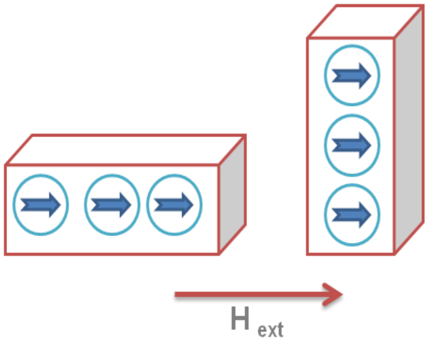

Figure 4.5 Schematic illustration of the size effect: different magnetization strength in samples with different thickness

MH-Dependence at T = 298K

Hysteresis-loops of the nanocrystalline Ni and Ni-15% Fe sample measured at T=298K are depicted in Figure 4.6. Hysteresis loops follow the same trend observed at T=2K magnetization curves. All samples possess low loss hysteresis loops. Nanocrystalline Ni-15% Fe sample exhibits the highest saturation magnetization and the lowest Coercivity. In the case where the field is applied parallel to the sample plane, nanocrystalline Ni and Ni-15% Fe sample reach saturations of 57.086 (emu/gr) and 90.029 (emu/gr), respectively at fields up to 1000 (Oe). For the measurements where the field is applied perpendicular to the sample's planes, nanocrystalline Ni and Ni-15% Fe samples reach saturation of 59.047 (emu/gr) and 84.737(emu/gr), respectively at fields as large as 10000 (Oe). Polycrystalline Ni sample, regardless of the direction of the applied field, reaches saturation at fields up to about 5000 (Oe).

The previous studies on the nanocrystalline Ni with grain sizes about 50 (nm) indicate saturation nearly at an applied field of about 0.2 (Tesla) and a final mass-magnetizations of 58.01 (Am^2/kg). [123].

No strong temperature-dependence on the magnetization was observed for samples, but the magnetization of the samples at T=2K was slightly higher than at T=298K for Ni-15%Fe samples. This observation is consistent with the results of another research study published by Weissmuller et al. [123]. The proposed reasons for lower saturation at higher temperatures are presence of higher thermal energy and more vibrations of the dipoles. These vibration effects reduce the exchange interactions among dipoles and leads to less alignment of the magnetic dipoles toward the field and a lower magnetization in the material.

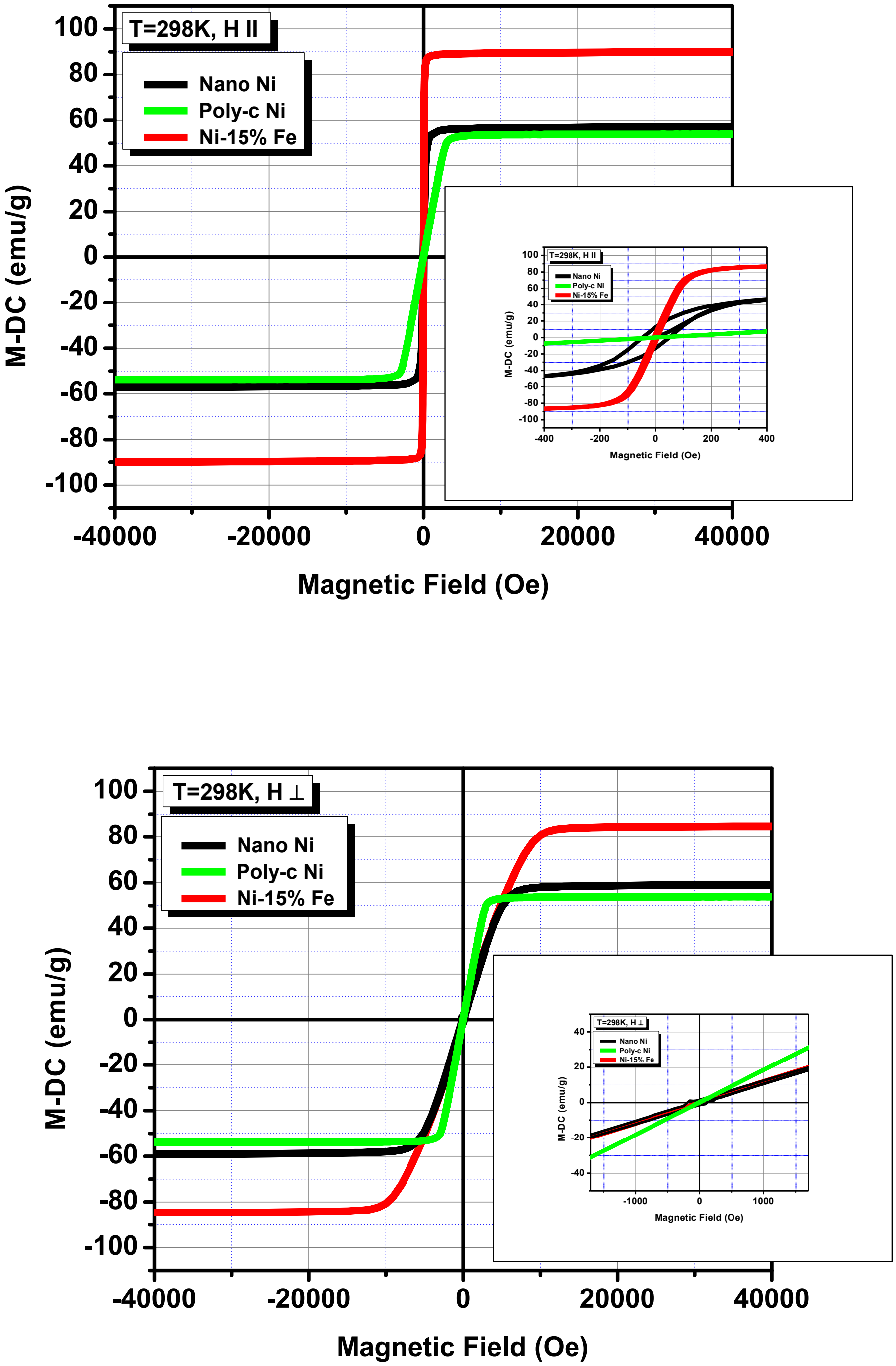

a)

b)

Figure 4.6 Hysteresis loops of polycrystalline Ni, nanocrystalline Ni and Ni-15% Fe samples where the magnetic fields up to 4 (Tesla) were applied a) parallel (φ = 0°) and b) perpendicular (φ = 90°) to the sample plane at T=298K.

4.2.2 Summary of Magnetic Properties

Table 4.2 presents the magnetic properties including saturation magnetization, remnant magnetization, coercivity, susceptibility, and squareness ratio of the Polycrystalline Ni, nanocrystalline Ni and Ni-15% Fe samples at temperatures of T=2K and 298K.

Table 4.2 Summary of Magnetic properties of Ni and Ni-15%Fe samples measured at fields parallel and perpendicular to the sample plane at T=2K and T=298K.

H || to sample's plane

T (K)	**Sample**	**M_S (emu/gr)**	**H_C (Oe)**	**M_r (emu/gr)**	**χ (10^{-5} emu/gr Oe)**	**Mr/Ms**
2	**Nano. Ni**	60.169	95.820	20.936	0.884	0.347
	Nano Ni-15% Fe	93.671	5.956	4.135	0.590	0.044
298	**Nano. Ni**	57.086	48.851	12.711	0.855	0.222
	Nano Ni-15% Fe	90.029	6.267	6.107	0.442	0.067

H ⊥ to sample's plane

T (K)	**Sample**	**M_S (emu/gr)**	**H_C (Oe)**	**M_r (emu/gr)**	**χ (10^{-5} emu/gr Oe)**	**Mr/Ms**
2	**Nano. Ni**	62.436	151.542	2.152	0.041	0.034
	Nano Ni-15% Fe	89.003	4.472	0.185	0.053	0.002
298	**Nano. Ni**	59.047	101.431	1.516	0.081	0.025
	Nano Ni-15% Fe	84.737	4.571	0.092	0.008	0.001

T (K)	Sample	M_S (emu/gr)	H_C (Oe)	M_r (emu/gr)	χ (10^{-5} emu/gr Oe)	Mr/Ms
2	**Poly-c Ni**	57.352	11.320	0.243	0.005	0.004
298	**Poly-c Ni**	53.897	13.023	0.288	0.006	0.005

Saturation magnetization: From Table 4.2 it can be noted that when the field is applied parallel to the sample plane at temperature T=2K, the Saturation magnetization of the sample containing Ni-15%Fe is highest (93.67 (emu/gr)), which is slightly higher in comparison with the ones at 89.003 (emu/gr) perpendicular applied field. The same trend is observed for the nanocrystalline Ni sample with Saturation magnetization of 60.169 (emu/gr) and 57.352 (emu/gr), respectively.

The saturation magnetization for nanocrystalline Ni measured in parallel and perpendicular applied fields at T=298K, is 57.086 (emu/gr) and 59.047 (emu/gr), respectively. These values slightly deviate from the M_S value for bulk Ni at room temperature given in the literature (58.5 (emu/gr)) [124]. Considering the fact that the error of the PPMS-9 instrument in measurement of magnetic moment is around 1%, such deviations may be due to error in the determination of the weight of the foils.

Overall, several trends are observed for the saturation magnetization of studied materials, including the fact that the saturation magnetization of the Ni-15%Fe is at all times larger than that of Ni sample. This increase in magnetization can be attributed to the strong effect of Fe in the Ni-15% Fe sample. The saturation magnetization of samples exhibits higher values at temperature 2K in comparison with T=298K.

Coercivity: from the coercivity values available in table 4.2 in both cases of parallel and perpendicular orientation of the applied fields, a strong decrease in coercivity with increasing iron content in nanocrystalline Ni-based alloys was observed. For the field applied parallel to the sample plane and measured at T=2K, the coercivity of Ni decreased from 95.82 (Oe) to 5.956 (Oe) for Ni-15%Fe. The same trend is observed for perpendicular case with values of 151.54 (Oe) and 4.472 (Oe) respectively. When considering measurement at higher temperature (T=298K), it is also noted that Coercivity of Ni and Ni-15%Fe exhibits decreasing values of 48.85 (Oe) to 6.267 (Oe) in the parallel applied field and 101.43 (Oe) to 4.571 (Oe) in the orientation of the sample perpendicular to the applied field. This trend can be explained by application of Herzer random anisotropy model (RAM): a decrease in H_C indicates an enhanced magnetic coupling with the consequence that the effective anisotropy constant K_{eff} is reduced further by averaging over a larger number of coupled grains. This model states that the coercivity is proportional to the grain size with D^6 and for the crystallite sizes <50 (nm), Coercivity decreases steeply with the decreasing grain size. Grain sizes of the nanocrystalline Ni and Ni-15%Fe alloys were measured being about 23 and 12 (nm). This explains the reason for the coercivity of the nanocrystalline Ni-15%Fe being much smaller than that of nanocrystalline Ni ones leading to excellent soft magnetic properties of Ni-15%Fe material.

Coercivity of the polycrystalline Ni sample at both temperature of T=2K and T=298K exhibit values as low as 11.32 (Oe) and 13.02 (Oe), respectively, which are lower than the corresponding values for nanocrystalline Ni samples. This may be due to the healing of imperfections at grain boundaries and interfaces after the annealing step (performed during the fabrication of polycrystalline Ni sample where the growth of crystallites is enhanced via an annealing process at Temperatures around 500^{o}C) as also suggested in another research study [125].

Squareness ratio SQ (Mr/Ms): According to the experimental data, the squareness, measured in nanocrystalline samples for the case where both the applied field is parallel and perpendicular to the sample plane, decreases with an increase in the iron content of the nanocrystalline deposit. Additionally, the squareness measured for the perpendicular applied field is always smaller than the one measured in a direction parallel to the sample plane. The difference between the squareness values for the two orientations suggests the existence of a planar anisotropy in the samples. However, a very characteristic feature in the small grain size regime is that due to RAM, if exchange interactions dominate over the random anisotropies, the squareness ratio should to be about $Mr/Ms \simeq 0.95$ and $D \simeq 0.6\ L_0$. The former is not observed in our experimental results. The reason for this is that the measurements in this research study were not corrected using the geometrical demagnetizing factors which results in superposition of the curves measured for the different orientations in the range of interest, and more reliable squareness ratios.

4.3 Anisotropy Measurements

In this Section, fitting of the experimental high field magnetization curves with the law of approach to saturation has been conducted which lead to further enhancement in obtaining more reliable saturation magnetization and effective anisotropy constants.

4.3.1 Law of Approach Saturation

Applying the law of approach to saturation to measure the magnetocrystalline anisotropy of nanocrystalline two phase materials was discussed earlier in Section 2.4.2 where the magnetization M is expressed as a function of the magnetic field:

$$M = M_s \left(1 - \frac{a_1}{\sqrt{H}} - \frac{a_2}{H^2} - \frac{a_3}{H^3} \dots\right) + \chi H \tag{2.22}$$

In order to test whether or not equation 2.22 can be applied to analyze the experimental data, the representations of M as a function of $1/\sqrt{H}$ and $1/H^2$ for the nanocrystalline Ni and Ni-15% Fe alloys and poly crystalline Ni in bulk are presented in Figures. 4.7 and 4.8. As mentioned earlier the $\frac{a_1}{\sqrt{H}}$ term is due to the defects. This term is dominant in low fields. The $\frac{a_2}{H^2}$ term is attributed to the magnetocrystalline anisotropy of the sample and is dominant in high fields.

By comparing these two Figures, it can be noted that the field dependence for the cases when the field is applied parallel to the sample is indeed different from the perpendicular one. In the same $1/\sqrt{H}$ or $1/H^2$ range, the perpendicular graphs show a much steeper slope than the parallel ones. For the parallel applied field, when the value of applied field is smaller than 400 (Oe), a field dependence according to a $1/\sqrt{H}$ -law is observed (Figure 4.7 (a)), whereas, according to Fig. 4.7 (b) in the field range 400 (Oe) -5 (kOe), a relation $1/H^2$-law is observed for the nanocrystalline Ni and Ni-15% Fe alloys. The trend is rather different for the perpendicular graphs. When the value of applied field is smaller than 6 (kOe), a field dependence according to a $1/\sqrt{H}$ -law is observed (Figure 4.7 (a)). Whereas, according to Figure 4.7 (a) in the field range 6 (kOe) - 10 (kOe), a relation $1/H^2$ -law is observed for the nanocrystalline Ni and Ni-15% Fe alloys.

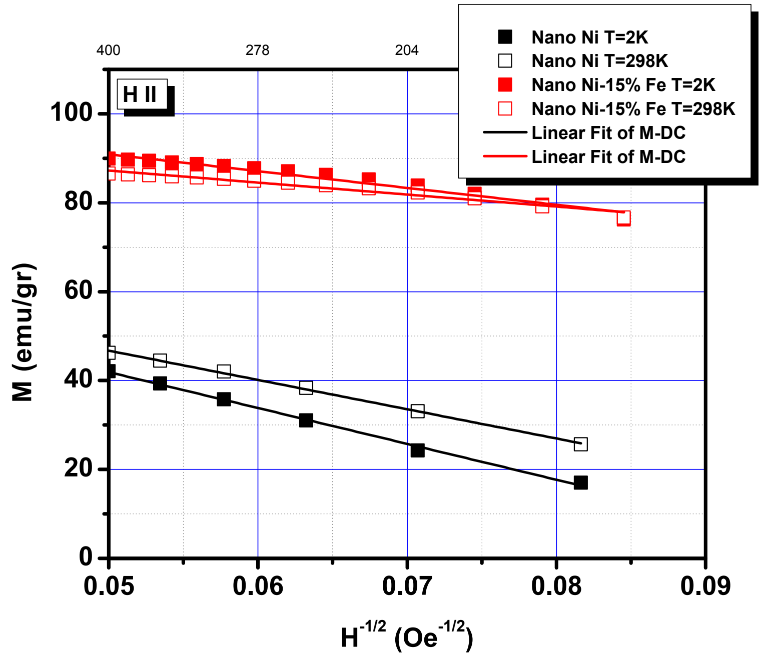

a)

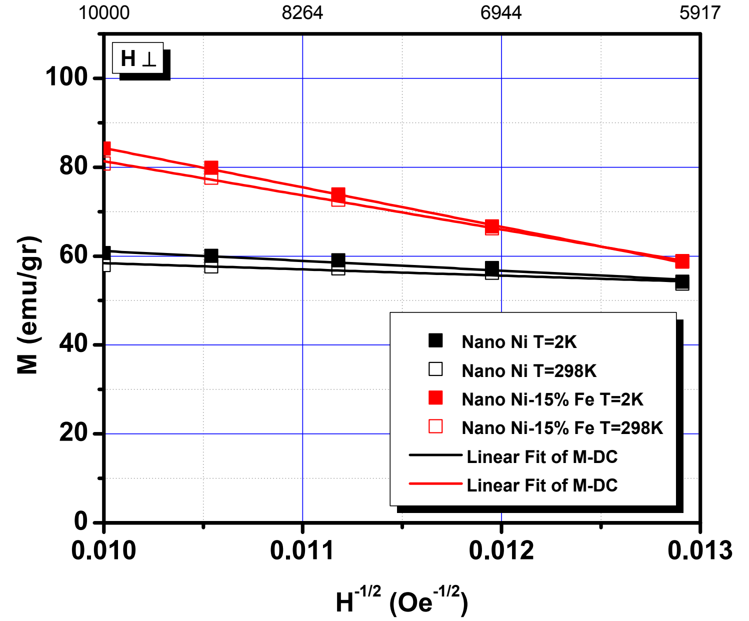

b)

Figure 4.7 The representation of M as a function of $1/\sqrt{H}$ for the nanocrystalline Ni and Ni-15% Fe alloys for field applied a) Parallel and b) perpendicular to the plane of the sample.

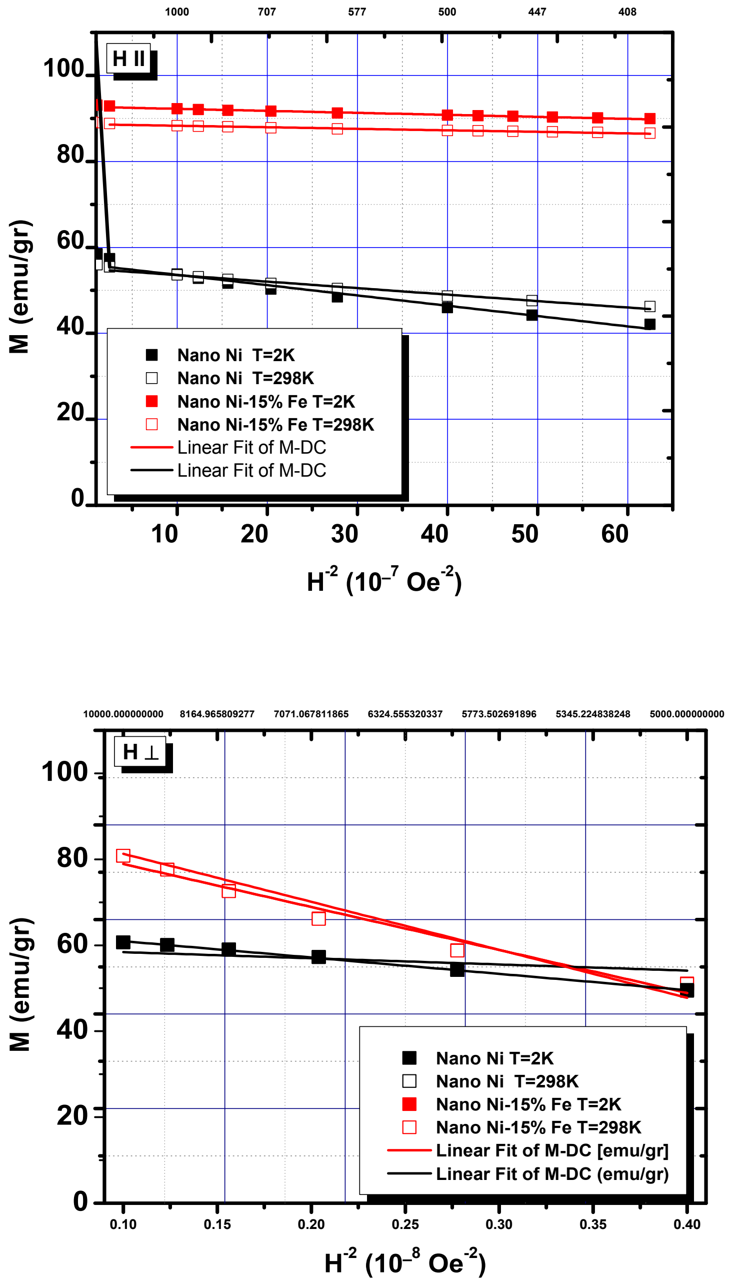

a)

b)

Figure 4.8 The representation of M as a function of $1/H^2$ for the nanocrystalline Ni and Ni-15% Fe alloys applied a) Parallel and b) perpendicular to the plane of the sample

Considering the results presented above, it was confirmed that equation 2.21 can be applied to fit the experimental data for this research study. a_1 and a_2 coefficients as well as saturation magnetization obtained from the experimental data are summarized in table 4.3.

Table 4.3 Structure parameter and magnetic data obtained from experimental Magnetization as function of $1/\sqrt{H}$ and $1/H^2$ curves.

H ‖ to sample's plane

T (K)	Sample	Ms From $1/\sqrt{H}$ (emu/gr)	Ms From $1/H^2$ (emu/gr)	a_1 ($\sqrt{Oe}$)	a_2 $(Oe)^2$
2	Nano. Ni	60.608	60.101	1.317	547411.856
	Nano Ni-15% Fe	93.791	93.572	0.425	268889.601
298	Nano. Ni	57.370	56.813	1.326	334448.160
	Nano Ni-15% Fe	90.032	89.723	0.692	456961.982

H ⊥ to sample's plane

T (K)	Sample	Ms From $1/\sqrt{H}$ (emu/gr)	Ms From $1/H^2$ (emu/gr)	a_1 ($\sqrt{Oe}$)	a_2 $(Oe)^2$
2	Nano. Ni	63.872	62.453	1.018	2662800.002
	Nano Ni-15% Fe	89.401	89.102	0.734	763955.915
298	Nano. Ni	60.098	58.799	3.368	1.171110.021
	Nano Ni-15% Fe	85.441	84.813	1.639	174383.644

T (K)	Sample	Ms From $1/\sqrt{H}$ (emu/gr)	Ms From $1/H^2$ (emu/gr)	a_1 ($\sqrt{Oe}$)	a_2 $(Oe)^2$
2	**Poly-c Ni**	57.393	57.407	0.097	443674.116
298	**Poly-c Ni**	54.067	53.883	0.634	424647.364

It is observed from the data presented in table 4.3 that saturation magnetization values obtained from two curves are quite consistent and the difference between observed and calculated values in magnetization is negligible (lower than 3%) which confirms the accuracy of the measurements.

The term $a_1/\sqrt{H}$: is related to a local anisotropy which originates from structural defects and nonmagnetic inclusions that causes nonuniform distribution in the direction of local magnetization (magnetocrystalline fluctuations). It is stated in Section 2.4.2 that in highly anisotropic compounds, the values of $a_1 \ll a_2$which is clearly observed from data recited in table 4. 3. The term a_2/H^2 is mainly due to non-compensated anisotropy energy in the sample.

4.3.2. Fitting the Experimental Data

In the next step, fitting the experimental magnetization curves with the law of approach to saturation was conducted. a_1 and a_2 coefficients as well as saturation magnetization were obtained from fitting. A least squares fitting procedure was applied for the best fit. The fitted curves are the optimum fits from which accurate values of coefficient and saturation magnetization M_S are obtained. Fitted curves are summarized in Figure 4.9- 4.11. It should be noted that in the parallel case, the fitting was performed nicely with the two first fitting component of the equation 2.22. However, for the case of perpendicular, the fittings curves did adapt to the experimental curves unless the third term $(\frac{a_3}{H^3})$ of higher order anisotropy components were incorporated in the fitting. In order to make a better sense of the role of each component in the equation 2.22, aside from fitting the experimental magnetization results with the full expression of law of approach to saturation, separate fittings are also separately conducted for each component (illustrated with colourful curves in Figures.4.9-4.10).

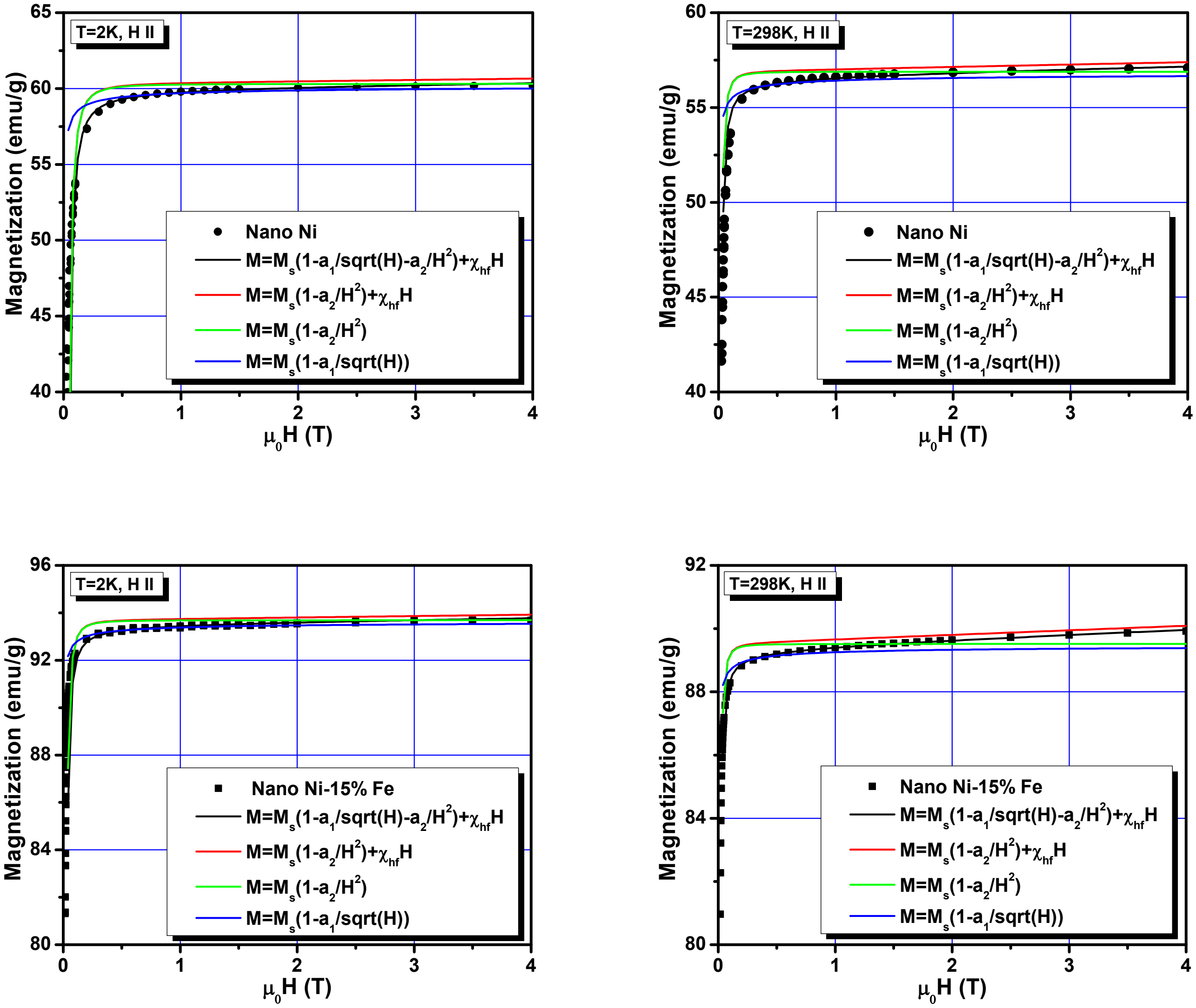

Figure 4.9 Experimental and modelled hysteresis loops of nanocrystalline Ni and Ni-15% Fe samples where the magnetic fields up to 4 (Tesla) were applied parallel to the sample plane at T=2K and T=298K.

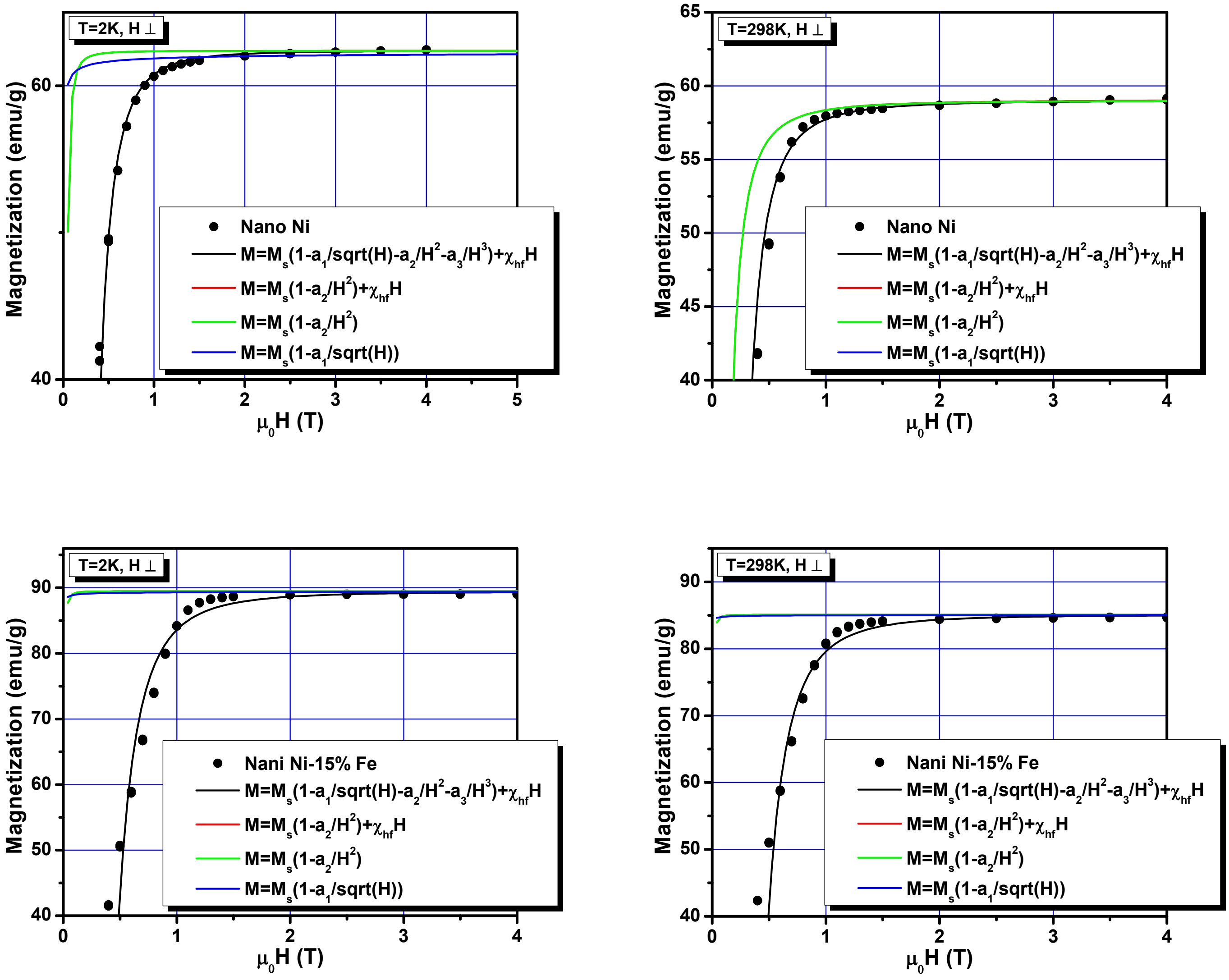

Figure 4.10 Experimental and modelled hysteresis loops of nanocrystalline Ni and Ni-15% Fe samples where the magnetic fields up to 4 (Tesla) were applied perpendicular to the sample plane at T=2K and T=298K.

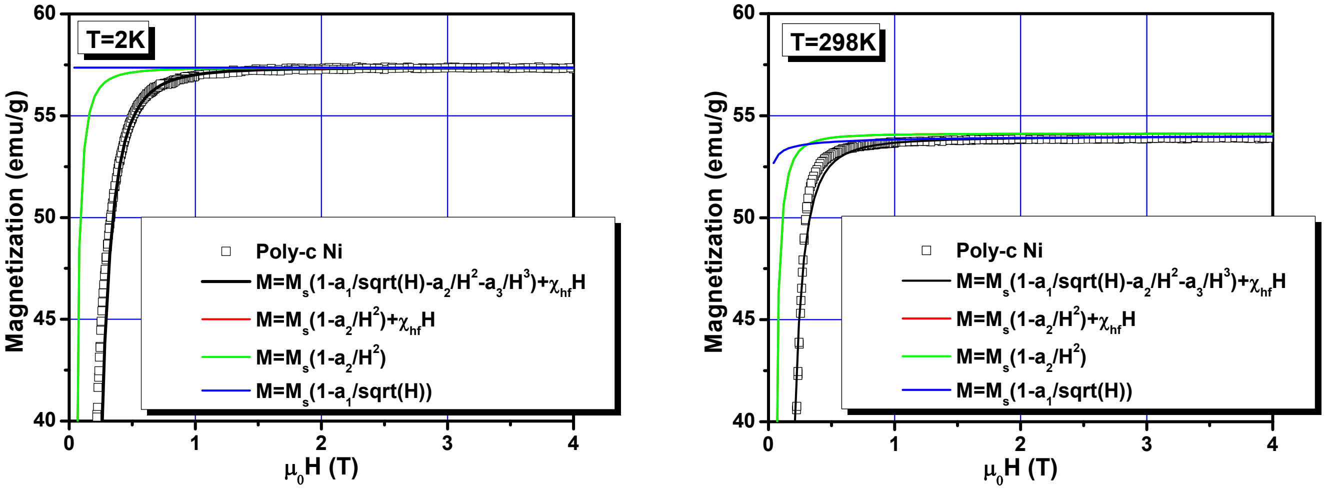

Figure 4.11 Experimental and modelled hysteresis loops of polycrystalline Ni samples at T=2K and T=298K.

It is worth mentioning that fitting the experimental curves with the full equation 2.22 encountered some difficulties initially due to the large number of coefficients involved, the experimental curve could be fitted with more than one combination of coefficients with the same accuracy. It can be observed from Figures 4.9- 4.11 that the experimental magnetization curves fit nicely with the full equation 2.22; however, in the case of Ni-15%Fe samples, there was inconsistency with the fitting where the experimental curves could not fit the expression of law of approach to saturation at fields smaller than 2 (Tesla). It was realized from TEM studies on Ni and Ni-15%Fe samples that Ni-15%Fe sample contains more structural defects such as twins, dislocations, stacking faults and triple junction than the Ni sample. These terms come to effect in lower fields and can affect the magnetization of the sample in great deal via pinning effect. One reason to this problem may be the very small average grain size of the Ni-15%Fe sample and the possible defects that are not included in the full expression. This may also point out the need for a new modified expression which explains the behaviour of binary nanocrystalline materials with grain sized below certain ranges as well. The new modified fitting components including a'_1 , a'_2 and a'_3, as well as saturation magnetization values are summarized in table 4.4.

Table 4.4 Optimized saturation magnetization and fitted parameters obtained from fitting the experimental data with equation 2.22

H ∥ to sample's plane				
T (K)	**Sample**	**Ms From Fitting (emu/gr)**	a'_1 ($\sqrt{\mathrm{Oe}}$)	a'_2 $(10^4\ \mathrm{Oe})^2$
2	**Nano. Ni**	60.308	1.017	5.745
	Nano Ni-15% Fe	93.686	0.325	0.318
298	**Nano. Ni**	56.891	0.826	5.235
	Nano Ni-15% Fe	89.515	0.292	0.224

H ⊥ to sample's plane					
T (K)	**Sample**	**Ms From Fitting (emu/gr)**	a'_1 ($\sqrt{\mathrm{Oe}}$)	a'_2 $(10^4\ \mathrm{Oe})^2$	a'_3 $(10^{10}\ \mathrm{Oe})^3$
2	**Nano. Ni**	62.371	0.008	6.541	2.506
	Nano Ni-15% Fe	89.471	0.189	0.888	6.406
298	**Nano. Ni**	59.013	0.072	6.424	1.601
	Nano Ni-15% Fe	85.094	0.110	0.496	6.367

T (K)	**Sample**	**Ms From Fitting (emu/gr)**	a_1' ($\sqrt{Oe}$)	a_2' **(10^5 Oe)^2**	a_3' **(10^9 Oe)^3**
2	**Poly-c Ni**	57.361	0.101	1.011	5.060
298	**Poly-c Ni**	54.124	0.534	0.941	2.043

4.3.3 Measuring Effective Anisotropy Constant (K_{eff})

As mentioned in Section 2.4.2, the coefficient a_2 is related to magnetocrystalline anisotropy. For cubic crystal materials, when this value is known, the effective anisotropy coefficient (K_{eff}) can be estimated from equation (2.24), Furthermore, having the K_{eff} value, the exchange length can be derived from equation 2.12:

$$\boldsymbol{L_{ex}} = \varphi \sqrt{\left(\frac{A}{K_{eff}}\right)} \tag{2.12}$$

It is well known from Herzer RAM that soft magnetic properties arise from the suppression of these local random anisotropies by exchange interactions. This mechanism becomes effective for grain sizes, D, smaller than the basic ferromagnetic exchange length (L_{ex}). Thus by calculating the L_{ex} and comparing it with the grain size, experimental results with RAM can be verified.

Table 4.5 includes the calculated K_{eff}, and the exchange length (L_{ex}) values of the polycrystalline Ni as well as the nanocrystalline Ni and Ni-15%Fe samples. It should be noted that the values of φ and A employed in calculating the $L_{ex,}$ were 0.64 (nm), and 0.75×10^{-6} (erg/cm^3), respectively and were obtained from a research study on electrodeposited nanocrystalline Ni [120].

Table 4.5 Anisotropy constants and ferromagnetic exchange length of nanocrystalline samples were for field applied parallel and perpendicular to the plane of the sample at T=2K and T=298K.

		H ‖ to sample's plane		H ⊥ to sample's plane	
T (K)	Sample	K_{eff} (10^5erg/cm^3)	L_{ex} (nm)	K_{eff} (10^5erg/cm^3)	L_{ex} (nm)
2	Nano. Ni	4.660	45.666	5.143	43.472
	Nano Ni-15% Fe	1.703	75.532	2.719	59.779
298	Nano. Ni	4.197	48.124	4.822	44.893
	Nano Ni-15% Fe	1.367	84.319	1.932	70.918

K_{eff} value of the polycrystalline Ni sample were measured to be 5.882×10^5 (erg/cm^3) respectively at T=2K and 5.354×10^5 (erg/cm^3) at T=298K. These values are in good agreement with the literature data for pure nickel, 5.7×10^5 (erg/cm^3) and confirms successful measurements on the pure nickel sample. The K_{eff} values of nanocrystalline samples are further investigated based on their composition and temperature of measurements as well as the orientation of the field.

Effective Anisotropy Constant at T = 2K

It is observed from calculated values in table 4.5 that regardless of the field orientation toward the sample, by addition of 15% Fe to nanocrystalline Ni, the effective anisotropy constant value has decreased. In the case where the field is parallel to the sample, K_{eff} decreased from 4.660×10^5 (erg/cm^3) to 1.703×10^5 (erg/cm^3).

It can be confirmed from the values of exchange length of Ni-15% Fe to be 75.532 (nm) > 12 (nm) (grain size) that the local magnetocrystalline anisotropy of the individual grains were to some extent averaged out in the alloy. One explanation for this effect is that by addition of Fe to Ni (when Fe content increases but remains small enough) Fe atoms sit into the Ni sites without large distortion of the lattice. Consequently this results in averaging out effect of the macroscopic anisotropy, where $K_{eff} < K_1$. The same trend is observed when the applied field is perpendicular to the sample.

It can be noted that K_{eff} value of Ni-15% Fe is about 2.719×10^5 (erg/cm^3) which is half of the value for the nanocrystalline Ni sample of 5.143×10^5 (erg/cm^3). This can be explained by the fact that L_{ex} in the Ni-15%Fe sample (59.779 (nm)) was bigger than its grain size, which resulted in domination of exchange interaction over the random orientations of the local anisotropy axis and averaging of the anisotropy constant.

Effective Anisotropy Constant at T = 298K.

The overall trend for the effective anisotropy constant at T=298K is the same as in T=2K. In the case where the field is applied parallel to the sample, by addition of 15% Fe to nanocrystalline Ni, the effective anisotropy constant value K_{eff} decreased from 4.197×10^5 (erg/cm^3) to 1.367×10^5 (erg/cm^3) and L_{ex} of nanocrystalline Ni-15% Fe and Ni were 84.319 (nm) > 12 (nm) and 48.124> 23 (nm), respectively. In measurements where the field was perpendicular to the sample plane, this value declined from 4.822×10^5 (erg/cm^3) to 1.932×10^5 (erg/cm^3).

One important observation about effective magnetic anisotropy constants is its variation with temperature. It is known from previous studies that the value of K_{eff} decreases with increasing temperatures and reaches very low values around the Curie temperature [126]. From the data presented in table 4.5, it is noted that the values of K_{eff} decreases following this trend. The value of K_{eff} calculated from field measurements conducted parallel to nanocrystalline Ni (Ni-15% Fe) at T=2K decreased from 4.660×10^5 (erg/cm^3) (1.703×10^5(erg/cm^3)) to 4.197×10^5 (erg/cm^3) (1.367×10^5 (erg/cm^3)) at T=298K. The measured K_{eff} values for the polycrystalline Ni sample shows more or less the same trend of decreasing K_{eff} values from 5.882×10^5 (erg/cm^3) to 5.354×10^5 (erg/cm^3). This emphasizes on the fact that this trend occurs regardless of the crystalline size or composition.

4.3.4 Correlation between K_{eff}, H_C and μ

Referring to Section 2.4.1, one of the most important predictions of the Herzer random anisotropy model was that the effective anisotropy and coercivity are related to the power of six of the grain size. The coercivity was mentioned to be related to the effective magnetocrystalline anisotropy via Equation (2.19) below:

$$H_C = P_c \frac{K_{eff}}{M_s} \tag{2.19}$$

It was also emphasized that the predicted D^6-dependence is well reflected in the coercivity and permeability data for grain sizes below about 40 (nm). Thus the relationship between H_C, μ, and K_{eff} are summarized as: $H_C \sim K_{eff}$ and $\mu \sim 1/ K_{eff}$.

To investigate the accuracy of the above relationship, the experimental values of coercivity and the values obtained from RAM expressions are compared against each other. Table 4.6 depicts the experimentally obtained for H_C and values of coercivity calculated on the basis of RAM approach for the nanocrystalline Ni and Ni-15% Fe samples. The permeability of the samples was also compared.

Table 4.6 The coercivity values obtained from experiments and RAM expressions in parallel and perpendicular applied fields at T=2K and T=298K

			H ‖ to sample's plane		**H ⊥ to sample's plane**	
T (K)	**Sample**	**D (nm)**	**H_C experiments (Oe)**	**H_C RAM (Oe)**	**H_C Experiments (Oe)**	**H_C RAM (Oe)**
2	**Nano. Ni**	23	95.820	574.472	151.542	503.661
	Nano Ni-15% Fe	12	5.956	211.778	4.472	126.682
298	**Nano. Ni**	23	48.851	524.122	101.431	599.149
	Nano Ni-15% Fe	12	6.267	158.222	4.571	106.394

It can be observed from the data provided in table 4.6 that coercivity values obtained experimentally and on the basis of RAM approach both decreases as the grain size of Ni (23 (nm)) decreases to 12 (nm) in Ni-15% Fe. Comparison of the coercivity values suggests that the magnetic behaviour of nanocrystalline Ni and Ni-15% Fe alloy system can be explained on the basis of random anisotropy mechanism, since by introduction of Fe to Ni, the grain size and the coercivity values regardless of the orientation of the sample in the applied field substantially decrease. The supporting reason to this behaviour is the reduction in the effective anisotropy constants from Ni to Ni-15%Fe sample while the exchange length is in the order of 2-3 grain sizes in this material. Aside from coercivity and exchange length values, the good matching between the fitting of the experimental data on the equation of the law of approach to saturation is a good proof of this suggestion according to previous research studies [54, 127, 128]. However, the coercivity values obtained from experimental data are much smaller than those obtained on the basis of RAM approach. The discrepancy between experimental results and the RAM based Coercivity values have been reported in previous research studies [129]. A research study on partially crystallized amorphous ribbons was done by V. Basso et al [130]. These researchers mentioned that the microstructure affects the hysteresis properties in such a way that the measured coercivity follows a fourth power dependence of mean grain size. The reason of this behaviour is mentioned to be the domain wall pinning by nanograins and some separate magnetization mechanisms that are supposed to be associated with the amorphous and crystalline phase [130]. In this case, the correlation length is controlled by amorphous phase (72%-92%) and nano-crystals are only contributing to the fluctuations in domain wall energy thereby acting as pinning centres. Salil Modak (2008) [129], stated that in case of Fe-Zr-Nb-B based nanocrystalline Ribbons and thin films, the magnetic behaviour is rather governed by the correlation length scale which is determined by the amorphous phase. The magnetic properties of these alloys seem to have a less strong dependence on average grain size with respect to the one expected in the framework of RAM approach where the correlation length is governed by the nanocrystalline phase [129].

With regard to the above mentioned approaches, two reasons are proposed to the discrepancy observed between experimental and RAM-based coercivity values in nanocrystalline Ni and Ni-15%Fe samples. The first reason may be the variation of the grain size not considered in the model. The grain size that is used in the model is average of 1000 grains, not all the grains are the same size and shape and some are strongly distorted. Therefore, the local magnetocrystalline anisotropy constant (K_1) and the exchange interactions (A), between the grains change. Nonetheless, the grain size dependence in equation 2.19 can act as a good guiding principle for most of the data. However, the systematic deviations from the theoretical D^6 dependence due to additional crystalline phases and magneto-elastic and induced anisotropies are not considered in RAM.

The precipitation of small fractions of Fe solute precipitate can drastically affect the soft magnetic properties although the grain size of the FCC crystallites may remain unchanged. It has been also reported that at grain sizes below about 15–20 (nm), the Magneto-elastic and induced anisotropies may result in vanishing or modified grain size dependence of coercivity and permeability.

From the permeability point of view, and by looking at the hysteresis loops, it can be inferred that the permeability of the nanocrystalline Ni-15%Fe is larger than nanocrystalline Ni. Since the permeability has an inverse relationship with the anisotropy constant, it is realized that there is a consistency within measurements, where the K_{eff} of nanocrystalline Ni-15%Fe is smaller than nanocrystalline Ni regardless of the orientation of the sample toward the applied field.

4.4 Magnetoresistivity Measurements

It was mentioned in Chapter 2 that the MR effect is generally observed in ferromagnetic metals and alloys, where the electrical resistivity depends on the magnetization direction M with respect to the electric current direction. Various orientations of the sample regarding the direction of the applied magnetic field were taken into account. In this research study, the MR is defined as:

$$\mathrm{MR}\% = \frac{\rho-\rho_{\perp}}{\rho_{\perp}}\times 100 \qquad (3.1)$$

Where $\rho_{\perp}$ is the maximum resistivity value when the sample is perpendicular to the magnetic field of 9 (Tesla).

4.4.1. Angular Dependent Magnetoresistivity

Magnetoresistance curve (MR%) of nanocrystalline Ni and Ni-15% Fe samples are presented in Figures. 4.12 (a) and (b), respectively. The data are taken for decreasing applied field after saturating the sample with a field of 9 (Tesla), ensuring that the sample consists of a single magnetic domain. The measurements were done in the transverse configuration, where the direction of the magnetic field was kept perpendicular to the direction of current in the plane of the sample.

It can be noted from Figure 4.12 (a), that the MR behaviour of the nanocrystalline Ni follows the traditional twofold symmetric MR in 360° range proposed by Döring [63]. This can be explained by a sinusoidal relation with maxima and minima where the current is respectively perpendicular and parallel to magnetization, respectively [63]:

$$\rho = \rho_{\perp} + (\rho_{\boldsymbol{II}} - \rho_{\perp})\boldsymbol{cos^2}\varphi \qquad (2.24)$$

Accordingly the angular dependence MR of nanocrystalline Ni shows a twofold symmetry with peaks at 90° and 270°, and valleys at 0° and 180°. Unlike what is expected, the twofold symmetric MR is not correlated with the microstructure confirmed by experimental observations reported in other research studies [63, 131, 132].

The reason to such twofold symmetric MR in Ni lies in the negative and positive MR effect in the material which is fundamentally due to electron-orbit interactions. Negative magnetoresistance happens when the resistivity decreases in the sample positioned transverse to the direction of the field as the field increases. In this case the s-band electrons have less opportunity to scatter into empty d-band states. However positive magnetoresistance occurs when the field is applied parallel to the direction of the current in the sample and therefore, due to this special orientation, electrons from the s-band find the opportunity to scatter as much as possible into empty d-bands and this leads to increasing the resistivity. Electron-orbit interactions like the energy of the electrons are continuous therefore the MR of the sample changes gradually when the sample rotates toward the magnetic field. Since the bands where the electron can scatter in are definite, MR of these states is also definite and the overall trend of angular dependence MR can be explained with a sinusoidal behaviour where resistivity continuously gets maximized and minimized.

The twofold symmetric MR of nanocrystalline Ni evolves to four fold symmetry with addition of 15% Fe to the electrodeposited sample, as displayed in Figure 4.12 (b).This phenomena, which contradicts with the traditional theory proposed by Döring, was observed on sputtered epitaxial films. The proposed reasons to this transformation differ from one researcher to another. To further explore the prime cause of this behaviour, the effect of several factors including strain, magnetic field, magnetocrystalline anisotropy and composition on the angular dependence of MR are investigated individually below.

The internal stresses were not measured in this research study; however it is an absolute fact that in nanocrystalline materials composed of very fine grains, the presence of strain in the grains is inevitable. Thus the probability that the strain may be a reason to the observed fourfold symmetry behaviour in Ni-15%Fe sample remains for further investigations.

In the case of magnetic field; it has been recently reported that the change in the magnetic field only distorts or changes the MR behaviour and does not lead to a fourfold symmetry [133]. Fourfold MR changes the shape of the angular dependence of MR with the decreasing temperature, which is considered to be a result of stronger magnetocrystalline anisotropy at low temperatures.

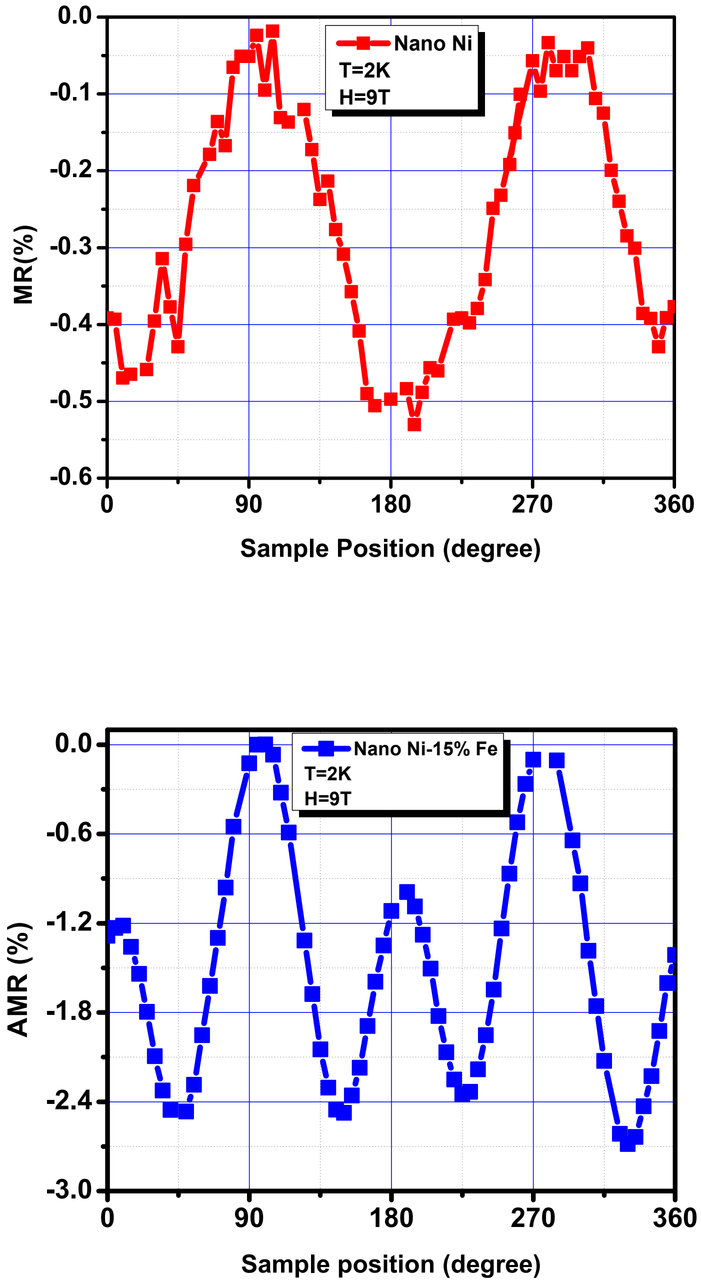

(a)

(b)

Figure 4.12 Orientation dependent MR of nanocrystalline (a) Ni and (b) Ni-15%Fe sample under the magnetic field of 9 (Tesla) at 2 K.

Magnetocrystalline anisotropy may be the other reason for the evolving from twofold symmetry to a fourfold symmetry. At high fields, the cubic magnetocrystalline anisotropy field superimposed onto the magnetic field aligns the spin moments near the high density grain boundaries of nanocrystalline grains, resulting in the additional sinusoidal oscillation in scattering and possibility of the electron transport along the hard or easy magnetization directions. With all the known facts as mentioned above, this observation is the first of its kind for soft nanocrystalline ferromagnets, and it is perceived that the origins and reasons for this fourfold symmetry MR may have more exclusive reasons which should be investigated in detail.

4.4.2 Field Dependent Magnetoresistivity

The angular variation of MR curves from 10 to 100° of MR curves for Ni-15%Fe sample was examined in a geometry in which the magnetic field was varied from a parallel position to a perpendicular position to the sample surface while the direction of the current was kept unchanged in the sample plane. The application of a magnetic field in the transverse (longitudinal) geometry causes a decrease (increase) in the resistance and this effect is called a negative (positive) magnetoresistance or transverse (longitudinal) magnetoresistance effect. The studies previously done on metallic materials such as Ni, confirms decreasing MR with increasing the applied field in the transverse configuration measurements and vice versa [134]. However the trends seen for Ni-15%Fe sample in different orientations toward the applied magnetic field are different.

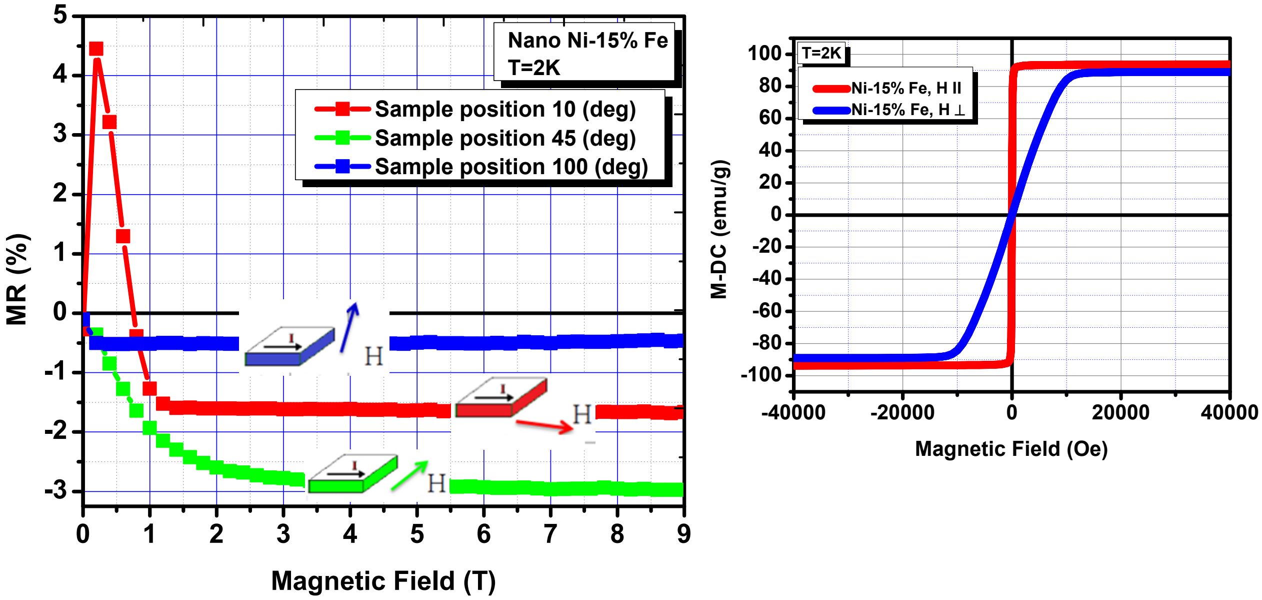

Figure 4.13 Field dependence MR of nanocrystalline Ni-15%Fe sample at various orientations of the sample toward the magnetic field and the corresponding hysteresis loops.

Figure 4.13 depicts the field dependence MR of nanocrystalline Ni-15%Fe sample at various orientations of the sample toward the magnetic field. It is observed that the sample oriented in different angles toward the field behaves differently as the field increases from 0 to 9 (Tesla).MR graph can be divided to two parts: low fields (Below 1

(Tesla)) and high fields (Between 1and 9 (Tesla)). While all samples at various tilt angles show moderately strong field-dependence, this orientation dependence tends to vanish as the field reaches 2 (Tesla) and above.

The change from the pure positive MR effect to the negative MR effect with the gradual change in the direction of applied field from parallel ($\theta = 10°$) to perpendicular ($\theta = 100°$) to sample plane is clearly seen in Figure 4.13. As the angle between the applied field and the sample plane increases, the perpendicular component of the field is created at the expense of the parallel one, and the saturation in the positive MR value is lost while a decreasing effect in the MR ratio emerges.

In the case of almost longitudinal magnetic field (10^o), by increasing the magnetic field, the resistivity sharply increases at low fields, reaches a maximum and then the negative MR effect in the sample becomes dominant above H ~ 0.4 (Tesla), while in the samples with different orientations (45^o and 100^o), the increase in the negative MR effect with increasing field is persisted with different slopes. The initial sharp increase in the positive MR effect (or in the resistance) for a small magnetic field increment (below »0.4 (Tesla)) is due to the domain wall motion and the rotation of magnetisation vector. The increase in the negative MR with high fields in these samples is attributed to the approach of magnetisation to a more complete saturation, indicating additional less 4s electron scattering. Similar to the magnetocrystalline anisotropy, MR effects are originated from the spin-orbit coupling. McGuire and Potter have also reported that the MR is thickness, grain size and deposition-dependant as well [135]. The observed MR effects in electrodeposited Ni-15%Fe in this study suggest that the highest effect of the spin-orbit coupling is seen in the low resistive sample orientation of $\theta = 45°$ among other sample orientations as an example which we could not encounter in literature.

Another way to investigate the MR effect is through the hysteresis loops. By recalling the hysteresis loops of the Ni-15%Fe samples in Section 4.2.1,(also shown in Figure 4.13) where the field is applied parallel and perpendicular to the sample plane and comparing the MR behaviour of samples at orientations of 10^o and 100^o toward the magnetic field, it is found that the smaller MR values corresponds to the higher initial permeability and saturation magnetization. This is due to the fact that the MR graph of the sample oriented 100^o toward the field has higher MR values than that of $10^{\,o}$. Thus, it can be inferred that the sample with smaller MR value has the excellent soft magnetic characteristics. On the other hand, it was observed from the magnetocrystalline anisotropy constant measurements of nanocrystalline Ni-15%Fe that, the value of K_{eff} is higher for the parallel orientation of the sample (which is assumed close to 10^o alignment in MR measurements) than for the perpendicular orientation. Since both anisotropic magnetoresistance and magnetocrystalline anisotropy originate from spin-orbit interaction, the anisotropic magnetoresistance can reflect the characteristics of magnetocrystalline anisotropy. Thus, lower MR of the sample oriented 10^o with respect to the applied field is due to its smaller magnetocrystalline anisotropy. Strain anisotropy can also be another reason to the MR behaviour which can be investigated furthermore.

The behaviour of the sample in 45^o can be further investigated. It is concluded that sample reaches saturations differently at different sample tilts, the way the saturation is approached is really interesting and it requires further studies.

.

Chapter 5

Conclusion and Outlook

This research study has been devoted to the study of magnetic properties and magnetotransport properties of nanocrystalline Ni and Ni-Fe alloys with Fe% < 20% composed of nanometre-sized grains. The improved understanding of the correlations between the structure, microtexture and magnetic behaviour are valuable for the understanding properties of other Ni-Fe alloys consisting of fine crystallites and should contribute to understanding of the design and optimization of material structure based on their magnetic properties. Nanocrystalline Ni and Ni-15%Fe alloys investigated in the present research study have been produced by electrodeposition. The nanocrystalline Ni and Ni-15%Fe consist of randomly oriented grains having an average size in the range of respectively ~23 and 12 (nm).

The observation and analysis of the results obtained from the above studies are enlisted as follows:

1. The phases of the deposits are confirmed by the XRD analysis using Rietveld refinement techniques. The respected Rwp-factors of Ni and Ni-15%Fe were respectively 1.709 and 1.710, which shows high accuracy of the phase refinement. The as-deposited Ni-15%Fe sample was comprised exclusively of a solid solution phase with lattice parameter of 0.354 (nm) which in comparison with nanocrystalline Ni sample of 0.352 (nm) shows small increase due to replacement of iron solutes in the Ni sites in lattice.
2. Texture analysis on nanocrystalline Ni and Ni-15%Fe revealed that texture components of Ni-15%Fe sample are the same as those measured in pure Ni. This is true since 15% of Fe content do not cause changes in alloy phase composition beyond the FCC structure. Both materials showed strong <100> fibre texture with some contribution of the <111> component. Addition of 15%Fe to the Ni though caused some refinement of the grain size and a reduction in the strength of both texture components. The calculated volume fraction of the <100> and <111> components for were 17.157 % and 3.201%, respectively for Ni and 22.032% and 6.160% for Ni-15%Fe and the rest was confined to random texture.
3. Magnetic measurements of the under study alloys showed that all samples exhibit low loss hysteresis loops with high permeabilities. The presence of 15%Fe in Ni leads to enhancement of the saturation magnetization (M_s) regardless of the direction of the applied field i.e the M_s shows an increase from 60.169 (emu/gr) in nanocrystalline Ni to 93.67 (emu/gr) in Ni-15%Fe sample. The M_s values of nanocrystalline Ni did not

vary much from polycrystalline Ni sample which confirmed again that the M_S is compositional dependent and not structural dependent. The permeability of the Ni-15%Fe samples was much higher than that of Ni samples. The larger permeability of the hysteresis loops measured at fields parallel to the sample than that of perpendicular ones were found to be due size effect and magnetocrystalline anisotropy. The values obtained for saturation magnetization in Ni-15%Fe measured at applied field parallel to the sample were slightly higher than that of perpendicular case which was attributed to the magnetocrystalline anisotropy effects in samples. No strong temperature–dependence on the magnetization observed for all samples, but that the magnetization of the samples at T=2K was slightly higher than T=298K. This observation was in consistency with the results produced previously by Weissmuller et al. [123]. The coercivity had a strong dependence on the composition and coercivity values of nanocrystalline Ni-15%Fe were in all cases smaller than that of nanocrystalline Ni samples. On the whole it was concluded that the magnetic properties of Ni-Fe nanocrystalline alloys are controlled by the fraction of the Fe content and magnetocrystalline anisotropy.

4. Using the law of approach to saturation, the effective magnetic anisotropy constants (K_{eff}) of the nanocrystalline Ni and Ni-15%Fe alloys were measured. It is found that the effective magnetic anisotropy constants decrease with introducing Fe to the Ni, and are larger than those of the corresponding polycrystalline Ni samples. Thus it

could be concluded that the local magnetocrystalline anisotropy of the individual Ni-Fe grains is largely averaged out in the nanocrystalline alloy.

5. We have found good agreement between RAM theory and experiment for nanocrystalline Ni and Ni-15%Fe samples with the highest magnetocrystalline anisotropy at ambient and low temperatures. At T=2K the K_{eff} of Ni-15%Fe samples were measured to be 1.703 $\times 10^5$ (erg/cm^3) and 2.719 $\times 10^5$ (erg/cm^3) at field parallel and perpendicular which were almost half of the values obtained for nanocrystalline Ni samples 4.660 $\times 10^5$ (erg/cm^3) and 4.197 $\times 10^5$ (erg/cm^3). With the same trend these values were smaller than K_{eff} values for polycrystalline Ni: 5.882$\times 10^5$(erg/cm^3) (measured) and 5.7$\times 10^5$ (erg/cm^3) (from the literature [136].Temperature dependence measurements showed that effective magnetic anisotropy constants decrease with increasing temperature. These results were consistent with the research study done previously [126].
6. The results for the ferromagnetic exchange length were in good agreement with the K_{eff} values confirming that for all samples L_{ex}>D. Comparison of the coercivity values suggested that the magnetic behaviour of nanocrystalline Ni and Ni-15% Fe alloy system can be explained on the basis of RAM, since by addition of 15%Fe to Ni, the coercivity values regardless of the orientation of the sample to the applied field showed significant decrease,
7. The angular and field dependent Magnetoresistivity of the nanocrystalline Ni and Ni-15%Fe were studied. It was found that for nanocrystalline Ni sample the MR

behaviour exhibits a twofold angular dependence, but the MR of Ni-15%Fe sample showed a fourfold symmetric behaviour. The proposed reason for this observation was that at high fields, the cubic magnetocrystalline anisotropy field superimposed onto the magnetic field aligns the spin moments near the high density grain boundaries of nanocrystalline grains, resulting in the additional sinusoidal oscillation in scattering possibility for the transport electrons along the hard or easy magnetization directions. The field dependence MR measured at various sample tilts toward the applied field, showed various trends. For samples oriented parallel and perpendicular to the applied field this trend could be explained by the magnetocrystalline anisotropy of the samples.

8. Over the course of this research several areas which could merit further study were noted. To have a complete understanding of the correlation between the magnetic and magnetotransport properties of electrodeposited nanocrystalline Ni and Ni-Fe alloys future research study on the following question is recommended:
   - Derive the differential scattering cross section to confirm the experimental results with the theory.
   - Estimate the grain boundary area electrical resistivity and compare it to the area derived from the average grain size determined from line broadening in XRD.
   - Study the effect of higher Fe composition alloys on the magnetotransport properties to reach a better understanding of the magnetic and MR properties.

References

---

1) J. L. McCrea, G. Palumbo, G. D. Hibbard, and U. Erb, Rev. Adv. Mater. Sci. 5 (2003)
2) W. Gong, H. Li, Z. Zhao, J. Chen, J. Appl. Phys. 69 (1991) 5119-5121.

3) A. Tsoukatos, H. Wan, G. C. Hadjipanayis, Nanostruct. Mater. 4 (1994) 49-59.

4) R. D. Shull, L. H. Bennett, Nanostruct. Mater. 1 (1992) 83-88.

5) M. Bedir, Ö. F. Bakkaloğlu, I. H. Karahan, and M. Öztaş, J. Phys. 66 (2006) 1093-1104.

6) F. R. Bento and L. H. Mascaro, Surf. Coat. Technol. 201 (2006) 1752-1756.

7) M. H. Seo, D. J. Kim, and J. S. Kim, Thin Solid Films. 489 (2005) 122-129.

8) S. Sam, G. Fortas, A. Guittoum, N. Gabouze, and S. Djebbar, Surf. Sci. 601 (2007) 4270-4273.

9) P. Fricoteaux and C. Rousse, J. Electroanal. Chem. 612 (2008) 9-14.

10) M. M. Ahadian, A. I. zad, E. Nouri, M. Ranjbar, and A. Dolati, J. Alloys. Comp. 443 (2007) 81-86.

11) Z. Zhao, The Transactions of Nonferrous Metals Society of China, 15 (2005) 897-901.

12) H. Gleiter, Prog. Mater. Soc. 33 (1989) 223-315.

13) W. Gong, H. Li, Z. Zhao and J. Chen, J. Appl. Pys. 69 (1991) 5119-5121.

14) H. E. Schaefer, H. Kisker, H. Kronmuller and R. Wurchum, Nanostruct. Mater. 1(1992) 523-529.

15) M. J. Aus, B. Szpunar, A. M. El-Sherik, U. Erb, G. Palumbo and K. T. Aust, Ser. Met. Mater. 27 (1992) 1639-1643.

16) H. Kisker, T. Gessmann, R. Wurschum, H. Kronmuller and H. E. Schaefer, Nanostruct. Mater. 6 (1995) 925-928.

17) X. Y. Qin, X. G. Zhu, S. Gao, L. F. Chi, and J. S. Lee, J. Phys. Condens. Matter. 14 (2002) 2605-2620.

18) R. M. Bozorth, Ferromagnetism, 1st ed., Wiley-IEEE Press., New York, (1951).

19) A.J. Freeman, R. Q. Wu, J. Magn. Magn. Mater. 104-107 (1992) 1-6.

20) S. Kobe, A. R. Fechmin, H. Nose, F. Stobiec ki, J. Magn. Mag. Mater. 60 (1986) 1-135.

21) J. C. S. Levy, J. Magn. Mag. Mater. 54- 47(1986) 277-278.

22) [http://www.magnets.bham.ac.uk/magneticmaterials/types.shtml]

23) [http://www.gitam.edu/eresource/Engg_Phys/semester_2/magnetic/types.htm]

24) B. D. Cullity, Introduction to Magnetic Materials, Addison-Wesley Publishing Company, Inc.: Reading, MA, (1972).

25) Y. K. Vekilov, E. I. Isaev, B. Johansson, Sol. State Commun. 133 (2005) 473-475.

26) A. S. Kotosonov, Carbon. 25 (1987) 613-615.

27) M. Gryzinski, J. Magn. Magn. Mater. 71(1987) 53-62.

28) [http://wwwchem.uwimona.edu.jm:1104/courses/magnetism.html]

29) F. Brailsford, physical principles of magnetism, D. Van Nostrand Company Ltd. London, (1966).

30) A. Sundaresan, C. N. R. Rao, Nano Today. 4 (2009) 96-106.

31) M. Fabrizio, C. Giorgi, A. Morso, Int. J. Eng Sci. 47 (2009) 821-839.

32) M. Knobel, M. Vazquez, L. Kraus, Handbook of magnetic materials, edited by K. H. J. Buschow, Vol. 15, Elsevier Science B.V., Amsterdam (2003).

---

33) Introduction of Magnetic Particle Inspection, “The Hysteresis Loop and Magnetic Properties”, NDT Resource Centre, Accessed May. 06, 2011. < http://www.ndted.org/EducationResources/CommunityCollege/MagParticle/Physics/HysteresisLoop.htm >

34) L. Yue, Z. Li, R. Kirby, D. R. Sellmye, Ultramicroscopy. 109 (2009) 1040-1043.

35) R. A. Taylor, J. P. Jakubovics, B. Astie, J. Degauque, J. Magn. Magn. Mater. 31-34 (1983) 970-972.

36) A. L. Brandl, J. C. Denardin, M. Knobel, M. E. R. Dotto, M. U. Kleinke, Physica B 320 (2002) 213-216.

37) D. H. Qin, M. Lu, and H.L. Li, Chem. Phys. Lett. 350 (2001) 51-56.

38) D. J. Craik and R. S. Tebble, Ferromagnetism and Ferromagnetic Domains, North-Holland Publishing Company: Germany, (1965).

39) C. Kittel, Rev. Mod. Phys. 21 (1949) 541-583.

40) R. Carey, E. D. Isaac, Magnetic domains and techniques for their observation, The English University Press Ltd, London (1966).

41) V. A. Zablotskii, K. V. Lamonova, Y. A. Mamalui, Physica B 205 (1995) 371-378.

42) K. Piotrowski, R. Szymczak, A. Maziewski, J. Magn. Magn. Mater. 15-18 (1980) 1541-1542.

43) A. A. Gavriliuk, A. Y. Mokhovikov, A. V. Semirov, A. L. Semenov, N. V. Turik, V.O. Kudrewcev, Jour. Non-Cryst. Solids. 354 (2008) 5230-5232.

44) M. T. Johnson, P. J. H. Bloemen, F. J. A. den Broeder and J de Vries, Rep. Prog. Phys. 59 (1996) 1409-1458.

45) N. Hasegawa, M. Saito, J. Magn. Soc. Japan 14 (1990) 313-318.

46) A. I. Gubanov, Fiz. Tverd. Tela2, 502 (1960) Sov. Phys. Solid State 2 (I960) 468-470.

47) Y. Yoshizawa, S. Oguma and K. Yamauchi, J. Appl. Phys. 64 (1988) 6044-6046.

48) K. Suzuki, N. Kataoka, A. Inoue, A. Makino, T. Masumoto, Mater. Trans. JIM 31 (1990) 743-746.

49) M. A. Willard, D. E. Laughlin, M. E. McHenry, D. Thoma, K. Sickafus, J. Gross, V. G. Harris, J. Appl. Phys. 84 (1998) 6773-6777.

50) G. Herzer, IEEE Trans. Mag. 25 (1989) 3327-3329.

51) G. Herzer, IEEE Trans. Mag. 26 (1990) 1397-1402.

52) G. Herzer, Scr. Metall. Mater. 33 (1995) 1741-1756.

53) G. Herzer, J. Magn. Magn. Mater. 294 (2005) 99-106.

54) W. F. Brown, J. Phys. Rev. 58 (1940) 736-743.

55) W. F. Brown, J. Phys. Rev. 60 (1941)139-147.

56) O. Heczko, P. Ruuskanen, IEEE Trans. Magn. 30 (1994) 513-515.

57) A. Sharbati, S. Choopani, A. Mousavi Azar, M. Sennad, Sol. State Commun. 150 (2010) 2218-2222.

58) T. Zhou, Z. Yu, Y. W. Du, J. Magn. Magn. Mat. 202 (1999) 354-358.

59) H. Kronmuller and H. GRIM, Physica 86-88B (1977) 805-806.

60) S. Chikazumi, Physics of Magnetism, Wiley, New York, (1964).

61) W. Thomson, Proc. Roy. SOC. 8 (1857) 546-550.

62) T. R. McGuire and R. I. Potter, IEEE Trans. Magn. 11 (1975) 1018-1038.

63) W. Döring, Ann. Phys. 424 (1938) 259-276.

64) R. Ramos, S. K. Arora, and I. V. Shvets, Phys. Rev. B, 78 (2008) 214402-214409.

65) R. Ramos, S. K. Arora, and I. V. Shvets, J. Appl. Phys. 105 (2009) 07B108-07B108-3.

66) A. W. Rushforth, K. Vyborny, C. S. King, K. W. Edmonds, R. P. Campion, C. T. Foxon, J. Wunderlich, A. C. Irvine, P. Vasek, V. Novak, K. Olejnik, J. Sinova, T. Jungwirth, and B. L. Gallagher, Phys. Rev. Lett. 99 (2007) 147207-147207- 4.

67) D. Wu, P. Wei, E. Johnston-Halperin, D. D. Awschalom, and J. Shi, Phys. Rev. B. 77 (2008) 125320-12532.

68) P. Li, E. Y. Jiang, and H. L. Bai, Appl. Phys. Lett. 96 (2010) 092502-146104.

69) M. Bibes, B. Martinez, J. Fontcuberta, V. Trtik, C. Ferrater, F. Sanchez, M. Varela, R. Hiergeist, and K. Steenbeck, J. Magn. Magn. Mater. 211 (2000) 206-211.

70) M. Bibes, V. Laukhin, S. Valencia, B. Martinez, J. Fontcuberta, O. Y. Gorbenko, A. R. Kaul, and J. L. Martinez, J. Phys.: Condens. Matter. 17 (2005) 2733-2740.

71) N. Myung, Bull. Korean Chem.Soc. 22 (2001) 994-998.

72) G. Palumbo, U. Erb and K.T. Aust, Scripta Metall. et Mater. 24 (1990) 2347-2350.

73) D. Osmola, P. Nolan, U. Erb, G. Palumbo and K.T. Aust. Phys. Stat. Sol. (a) 131 (1992) 569-575.

74) I. Brooks and U. Erb. Scripta Mater. 44 (2001) 853-858.

75) B. Szpunar, L.J. Lewis and I. Swainson. Phys. Rev. B 60 (1999) 10107-10113.

76) F. R. Bento and L. H. Mascaro, Surf. Coat. Technol. 201 (2006) 1752-1756.

77) M. Schlesinger and M. Paunovic "Modern Electroplating", 4th Ed. edited by, John Wiley & Sons, INC. (2000).

78) J. K. Dennis, T. E. Such, Ed. Newnes-Butterworths, "Nickel and chromium plating", London, (1972).

79) R. Oriňákova, A. Turoňová, D. Kladeková, M. Gálová, R. M. Smith, J. Appl. Electrochem. 36 (2006) 957-972.

80) A. Brenner, Electrodeposition of Alloys, Vol. 1 and 2, Academic Press, New York and London, (1963).

81) H. Dahms, I. M. Croll, J. Electrochem. Soc. 112 (1965) 771-775.

82) S. Hessami, C. W. Tobias, J. Electrochem. Soc. 136 (1989) 3611-3616.

83) M. Matlosz, J. Electrochem. Soc. 140 (1993) 2272-2279.

84) D. Landolt, Electrochim. Acta. 39 (1994) 1075-1090.

---

85) G. S. Georgiev, V. T. Georgieva, W. Plieth, Electrochim. Acta. 51 (2005) 870-876.

86) A. Ispas, H. Matsushima, W. Plieth, A. Bund, Electrochim. Acta. 52(8) (2007) 2785-2795.

87) S. N. Srimathi, S. M. Mayanna and B. S. Sheshadri, Surf. Technol. 16 (1982) 277-322.

88) M. Alper, H. Kockar, H. Kuru, T. Meydan, Sens. Actuators A Phys. 129 (2006) 184-187.

89) H. Kockar, M. Alper, H. Kuru, T. Meydan, J. Magn. Magn. Mater. 304 (2006) e736-e738.

90) M. H. Seo, D. J. Kim, and J. S. Kim, Thin Solid Films, 489 (2005) 122-129.

91) H. Dahms and I. M. Croll, J. Electrochem. Soc. 112 (1965) 771-775.

92) S. Hessami, C. W. Tobias, J. Electrochem. Soc. 136 (1989) 3611-3616.

93) L. Tiancheng, L. Zhichao, and L. Peng, Rare Metals, 25 (2006) 484-488.

94) M. Matlosz, J. Electrochem. Soc. 140 (1993) 2272-2279.

95) W. Plieth, J. Solid State Electrochem. 8 (2004) 338-345.

96) H. Li and F. Ebrahimi, Mater Sci Eng. A, 347 (2003) 93-101.

97) A. Afshar, A. G. Dolati, and M. Ghorbani, Mater Chem Phys. 77 (2002) 352-358.

98) Y. M. Yeh, G. C. Tu, and T. H. Fang, J. Alloys Comp. 372 (2004) 224-230.

99) [http://chemsoc.velp.info/alloys.php?elementno=28&index=7]

100) R. Abdel-Karim, Y. Reda, M.Muhammed, S. El-Raghy, M. Shoeib, and H. Ahmed, J. Nanomater. 2011 (2011)1-8.

101) M. Bedir, O. F. Bakkalogˇlu, I. H. Karahan, and M. Oztas Pramana, J. Phys. 66 (2006) 1093-1104.

102) F. Czerwinski, J.A. Szpunar and U. Erb, J. Mater. Sci. Mater. Electron. 11 (2000) 243-251.

103) E. P. Wohlfarth, ed., Ferromagnetic Materials, vol. 3, North-Holland Publishing Co., Amsterdam (1982).

104) X. Y. Qin, J. G. Kim and J. S. Lee, Nanostruct. Mater. 11 (1999) 259-270.

105) C. Cheung, F. Djuanda, U. Erb, G. Palumbo, Nanostruct. Mater. 5 (1995) 513-523.

106) C. Cheung, G. Palumbo, U. Erb, Scr. Metall. Mater. 31 (1994) 735-740.

---

107) M. Thuvander, M. Abraham, A. Cerezo, G.D. Smith, Mater. Sci. Technol. 17 (2001) 961-970.

108) H. Q. Li, F. Ebrahimi, Acta Mater. 51 (2003) 3905-3913.

109) U. Erb, K.T. Aust, G. Palumbo, J. McCrea, F. Gonzalez, in: T.S. Srivatsan, R. Varin, K.A. Khor (Eds.), Proc. 6th Intl. Symp. on Processing and Fabrication of Advanced Materials IX ASM International, Materials Park, OH, (2001) 253-262.

110) F. Czerwinski, H. Li, M. Megret, J. A. Szpunar, D. G. Clark, U. Erb, Scripta Mater. 37 (1997) 1967-1972.

111) D. L. Beke, Mat. Sci. Forum, 225-227 (1996) 701-706.

112) C. Cheng, M. J. Aus, U. Erb, J. McCrea and G. Palumbo, proc. 6th Intl. Conf. on Nanostructured Materials NANO 2002, Rutgers Univ, NJ, Nanotechnology Enterprises Inc, CD-ROM.

113) F. Czerwinski, J. A. Szpunar and U. Erb, J. of Mater. Sci.: Mater. Elec. 2 (2000) 243-251.

114) I. Z. Rahman, A. A Gandhi, M. V. Khaddem-Mousavi, T. F. Lynch, M. A. Rahman, J. Phys.: Conference Series, 61 (2007) 336-340.

115) Eric Lifshin, X-Ray Characterization of Materials, Wiley-VCH, Weinheim, (1999).

116) P. Esther, C. J. Kennady, and P. Saravanan, J. Sol. State Chem. 182 (2009) 2796-2800.

117) H. M. Rietveld, Profile refinement method for nuclear and magnetic structures. J. Appl.

Crystallogr. 2 (1969) 65-71.

118) S. Sam, G. Fortas, A. Guittoum, N. Gabouze, and S. Djebbar, Surf. Sci. 601 (2007) 4270-4273.

119) A. Ispas, H. Matsushima,W. Plieth, and A. Bund, Electrochem. Acta, 52 (2007) 2785-2795.

120) E. Kita, N. Tsukuhara, H. Sato, K. Ota, H. Yangaihara, H. Tanimoto and N. Ikeda: Appl. Phys. Lett. 88 (2006) 152501(1)-(3).

121) F. Ebrahimi and, H. Q. Li, Rev. Adv. Mater. Sci. 5 (2003) 134-138.

122) H. J. BUNGE, Texture Analysis in Materials Science, Butterworth, London (1982).

123) J. Weissmuller, A. Michels, J.G. Barker, A. Wiedenmann, U. Erb and R.D. Shull, Phys Rev. B 63 (2001) 214414 (1)-(18).

124) H. Danan, A. Herr, and A. J. P. Meyer, J. Applied. Sci. 39 (1968) 659-670.

125) H. Kisker, T. Gessmann, R. Wurschum, H. Kronmüller, and H. E.Schafer, Nanostruct. Mater. 6 (1995) 925-928.

126) Y. J. Zhang, Z. Wang, K. Y. He, H. H. Zhao, L. Z. Cheng, H. C. Yang, Acta Metallurgica Sinica 14 (2001) 267-270.

127) Z. Q. Jin, W. Tang, J. R. Zhang, H. X. Qin, and Y.W. Du, Eur. Phys. J. B 3 (1998) 41-44.

128) S.V. Andreev, M. I. Bartashevich, V. I. Pushkarsky, V. N. Maltsev, L. A. Pamyatnykha, E. N. Tarasov, N. V. Kudrevatykh, T. Goto, .J. Alloys Comp. 260 (1997) 196-200.

129) Salil Modak, PhD Thesis, Contribution to the Study of Magnetic Properties of Fe-Zr-Nb-B based nanocrystalline Ribbons and Thin Films, Cachan, Ecole Normale Superieure de Cachan, France (2008).

130) V. Basso, G. Bertotti, P. Duhaj, E. Ferrara, V. Haslar, L. Kraus, J. Pokorny, K. Zaveta
J.Magn. Magn. Mater. 157-158 (1996) 217-219.

131) W. Döring and G. Simon, Ann. Phys. 460 (1960) 373-387.

132) T. Uemura, Y. Imai, M. Harada, K. Matsuda, and M. Yamamoto, Appl. Phys. Lett. 94 (2009) 182502-(1)-(3).

133) P. Li, C. Jin, E. Y. Jiang, and H. L. Bai, J. Appl. Phys. 108 (2010) 093921-(1)-(5).

134) C.W. Heaps, Phys. Rev. 55 (1939) 1069-1071.

135) T. R. McGuire and R. I. Potter, IEEE Trans. Magn. Mag. II (1975) 1018-1038.

136) C. J. Gadsden, and H. Heath, Sol. State Commun. 20 (1976) 951-952.